Contents lists available at ScienceDirect

Arabian Journal of Chemistry

journal homepage: www.ksu.edu.sa

Original article

Enhanced sonophoto-catalytic and adsorption capabilities of Fe_3O_4@MC/MWCNT-CuO/Ag for petrochemical organic pollutants degradation from industrial process streams

Saeed Rajabi [a,b], Hassan Hashemi [c,*], Mohammad Reza Samaei [c], Alireza Nasiri [d], Abooalfazl Azhdarpoor [c], Saeed Yousefinejad [e]

[a] Student Research Committee, Shiraz University of Medical Sciences, Shiraz, Iran
[b] Department of Environmental Health Engineering, School of Health, Shiraz University of Medical Sciences, Shiraz, Iran
[c] Research Center for Health Sciences, Institute of Health, Department of Environmental Health Engineering, School of Health, Shiraz University of Medical Sciences, Shiraz, Iran
[d] Environmental Health Engineering Research Center, Kerman University of Medical Sciences, Kerman, Iran
[e] Department of Occupational Health and Safety Engineering, School of Health, Shiraz University of Medical Sciences, Shiraz, Iran

ARTICLE INFO

Keywords:
Advanced oxidation process
Catalytic degradation
Hybrid nanostructure
Persistent organic pollutant
Water purification

ABSTRACT

To address the problem of petrochemical organic pollutants in water, specifically monoethylene glycol (MEG) present in industrial process streams, in this research, we synthesized and evaluated a multifunctional nanocomposite, Fe_3O_4@MC/MWCNT-CuO/Ag. The nanocomposite was produced by combining magnetic Fe_3O_4 nanoparticles, methylcellulose (MC), multi-walled carbon nanotubes (MWCNTs), and CuO/Ag nanoparticles by an integrated synthesis process. A consistent dispersion of nanoparticles, with diameters ranging from 30-40 nm, was discovered by FESEM analysis, showing effective integration without aggregation. Effective synthesis was demonstrated by well-doped and evenly dispersed CuO and Ag nanoparticles. Functional groups that improve electrostatic interactions with contaminants hence enhancing catalytic performance and adsorption efficiency, were validated by FTIR analysis. XRD indicated an unchanged crystal structure with an average crystallite size of 8.67 nm. The anticipated elemental composition was verified by EDS & mapping. A VSM study revealed magnetic characteristics (9.33 emu/g) that simplify nanocomposite separation and reuse. TGA proved thermal stability to be up to 600 °C. A BET study showed a highly specific surface area of 67.661 m^2/g, enhancing adsorption. According to DRS and PL studies, the bandgap was lowered by 1.31 eV, which led to better optical absorption. The nanocomposite exhibited notable MEG removal efficiency, with 72 % in adsorption, 65 % in photocatalysis, and 56 % in sonocatalysis. This makes it a promising alternative for the remediation of organic pollutants in water treatment.

1. Introduction

Industrial operations introduce a plethora of organic substances through manufacturing processes and inadequate waste disposal methods to the ecosystem. Organic pollutants manifest varying levels of persistence and toxicity contingent upon their chemical makeup and environmental circumstances (Hawash et al., 2023; Malakootian et al., 2015; Akhgar et al., 2011; Akhgar et al., 2012). Many organic compounds exhibit resilience to breakdown and can endure in aquatic environments for extended durations, leading to their accumulation in aquatic organisms and amplification along the food chain. Additionally, certain organic pollutants like monoethylene glycol (MEG) exert adverse effects on human health, spanning from acute toxicity to chronic ailments, including carcinogenic, mutagenic, and endocrine-disrupting characteristics (Tripathi et al., 2023).

Polyester fibers, polyethylene terephthalate, and antifreeze production for automobiles and airplanes all rely on MEG. In addition, MEG is widely used in the natural gas extraction procedures carried out at gas

Peer review under responsibility of King Saud University.
* Corresponding author.
E-mail addresses: saeedrajabi27@gmail.com, saeedrajabi@sums.ac.ir (S. Rajabi), h_hashemi@sums.ac.ir (H. Hashemi), mrsamaei@gmail.com (M.R. Samaei), nasiri_a62@yahoo.com, ARNasiri@kmu.ac.ir (A. Nasiri), azhdarpoor@sums.ac.ir (A. Azhdarpoor), yousefinejad.s@gmail.com (S. Yousefinejad).

https://doi.org/10.1016/j.arabjc.2024.105994
Received 6 May 2024; Accepted 15 September 2024
Available online 16 September 2024

refineries. The main reason for its occurrence in water bodies is its extensive utilization in recycling operations at gas refineries and its use in diverse industrial operations, including petrochemical manufacture (Elreedy et al., 2017; Moradalizadeh et al., 2013; Zarandi et al., 2020). Given the complexity and variety of the contaminants, removing such organic pollutants from water and wastewater is difficult. Conventional treatment techniques such as coagulation, filtration, and disinfection typically face challenges in removing these substances, especially those with poor solubility and complicated chemical structures. The emergence of novel pollutants and the concurrent existence of many contaminants in water add complexity to the treatment process, underscoring the need for sophisticated treatment technology (Mondal et al., 2023; Pathania et al., 2016; Giahi et al., 2019; Sharma et al., 2017; Pathania et al., 2011).

Adsorption and catalysis processes are integral to mitigating the global environmental challenges posed by organic pollutants in aqueous solutions. Adsorption, extensively utilized in water and wastewater treatment, entails the adherence of contaminants onto solid materials, termed adsorbents (Yahya et al., 2018; Mehdizadeh et al., 2022; Maleky et al., 2022; Nasiri et al., 2022; Nasiri et al., 2022; Shirkhanloo et al., 2021; Shirkhanloo et al., 2022). This mechanism hinges on both physical and chemical interactions between the adsorbate molecules and the adsorbent surface, resulting in the extraction of contaminants from the aqueous medium. A myriad of materials, such as activated carbon, clay minerals, zeolites, and metal oxides, have been explored as adsorbents for organic pollutants due to their substantial surface area, porosity, and affinity for organic compounds (Adar et al., 2022; Rajabi et al., 2024; Hashemi et al., 2023; Rahimi et al., 2024; Rajabi et al., 2024).

Using catalysts in chemical processes speeds up the transformation of contaminants into inert or less hazardous compounds. Organic pollutant elimination catalytic techniques usually aim to degrade or convert pollutants into less dangerous and simpler forms (Mirnasab et al., 2021; Azarshab et al., 2024; Sabok-khiz et al., 2024). Advanced oxidation processes (AOPs), such as photocatalytic and sonocatalytic processes, leveraging catalysts like metal oxides, metal complexes, and nanomaterials, prove highly effective in decomposing stubborn organic pollutants by generating reactive oxygen species (Dong et al., 2022; Yazdanpanah et al., 2023).

The synergistic effect of adsorption and catalysis dramatically enhances the efficacy of organic pollutant removal from water. Catalysis converts contaminants into inert substances, while adsorption accumulates them on surfaces (Bello and Raman, 2019). The large surface area and catalytic features of silver nanoparticles make them very efficient in facilitating pollutant degradation via redox reactions and strong surface plasmon resonance (SPR) behavior. This SPR improves the absorption of light and the generation of electron-hole pairs, which are crucial for the process of photocatalysis (Yeshchenko et al., 2012; Alibeigi et al., 2021; Okeowo et al., 2020; Albukhari et al., 2019). Copper oxide (CuO) nanoparticles possess notable adsorption and catalytic capabilities, enhanced by their semiconductor characteristics, which contribute to the improvement of photocatalytic and sonocatalytic efficiency. This comprehensive method effectively tackles complex wastewater compositions, including many pollutants (Ighalo et al., 2021; Chauhan et al., 2020).

Conversely, iron oxide (Fe_3O_4) nanoparticles "also known as ferrites" offer magnetic properties that facilitate their easy separation and retrieval from aqueous solutions, rendering them highly desirable for adsorption purposes (Karami et al., 2024; Gharaghani et al., 2024). When integrated with methylcellulose (MC) and multi-walled carbon nanotubes (MWCNTs), these nanoparticles form nanocomposites with augmented adsorption and catalytic characteristics (Peng et al., 2018; Fadaei et al., 2017; Haghshenas et al., 2021). Since MWCNTs are made of many graphene layers arranged in a tubular form, one of their most important characteristics is their remarkably large surface area per unit mass. Its large surface area makes it easier for reactant molecules to engage with the many active sites it offers for catalytic reactions. MWCNTs are highly conductive in addition to having a large surface area, which facilitates effective charge transfer during catalytic reactions (Rong et al., 2022; Golbabai et al., 2013; Kahkha et al., 2020; Soleymani et al., 2020). Because MWCNTs may help transport electrons to and from catalytic sites, improving reaction kinetics, this conductivity is especially beneficial for electron transfer processes. The prevention of aggregation and enhancement of dispersion achieved by attaching these nanoparticles onto the MWCNT surface result in increased catalytic activity and overall system stability. Furthermore, MWCNTs themselves have inherent catalytic activity, particularly in redox activities or reactions involving carbon-based molecules. The undesirable process known as "charge carrier recombination" occurs when photogenerated electrons and holes join again before engaging in catalytic reactions, decreasing the efficiency of the catalytic process. MWCNTs enhance the efficiency and performance of catalytic processes, especially those that depend on light-driven mechanisms like photocatalysis, by efficiently reducing charge carrier recombination (Gui et al., 2015). MC, being a biocompatible and biodegradable polymer, serves as a stable matrix for nanoparticle dispersion, averting aggregation and enhancing pollutant accessibility (Haghshenas et al., 2021). MWCNTs, renowned for their high aspect ratio and conductivity, further bolster the adsorption capacity and catalytic performance of the nanocomposites (Huang et al., 2017; Rajabi et al., 2022).

Incorporating Ag, CuO, and Fe_3O_4 nanoparticles into the MC/MWCNT composite resulted in the development of a highly efficient nanocomposite for eliminating organic pollutants from water. This novel integration focused on the distinct characteristics of each constituent, presenting a hopeful approach to the serious problem of ecological contamination. Integrating Ag, CuO, and Fe_3O_4 nanoparticles into a composite of methylcellulose and multi-walled carbon nanotubes was the focus of our investigation into the synergistic effects. The present study aimed to demonstrate the enhanced effectiveness of Fe_3O_4@MC/MWCNT-CuO/Ag nanocomposites in purifying aqueous solutions by analyzing their elevated adsorption and catalytic capabilities. The novelty of this research consisted of its thorough approach to developing and evaluating a versatile nanocomposite, which offers an effective and environmentally friendly strategy for purifying water and addressing pollution.

2. Materials and methods

2.1. Chemicals

Various metal salts in analytical grade, such as copper nitrate trihydrate ($Cu(NO_3)_2{\cdot}3H_2O$), iron (III) chloride hexahydrate ($FeCl_3{\cdot}6H_2O$), silver nitrate ($AgNO_3$), and iron (II) chloride tetrahydrate ($FeCl_2{\cdot}4H_2O$), were procured from Merck Co. for the study. Additionally, other chemicals were sourced from the Sigma Aldrich store, including methylcellulose (MC), sodium hydroxide (NaOH), ammonium hydroxide (NH_4OH 25 %), and multi-wall carbon nanotubes (MWCNT).

2.2. Preparation of Fe_3O_4@MC/MWCNT-CuO/Ag

2.2.1. Fe_3O_4@MC/MWCNT

The synthesis of Fe_3O_4@MC/MWCNT involved a sophisticated microwave-assisted co-precipitation technique. The first step was to prepare a solution by dissolving 2.7 g of $FeCl_3{\cdot}6H_2O$ and 1 g of $FeCl_2{\cdot}4H_2O$ in 100 mL of distilled water. Methylcellulose (0.5 g) was introduced into the solution, and the mixture was stirred at room temperature. Subsequently, NaOH was meticulously added dropwise to the solution for an hour until reaching a pH of 11. The last step was adding 0.12 g of MWCNTs to the suspension. The resulting mixture was then subjected to microwave irradiation (using a SAMSUNG model, 2450 MHz, 450 W) for 15 min, divided into three intervals of 5 min each. Following irradiation, the formation of a black precipitate ensued, which was subsequently washed multiple times with distilled water and

subsequently dried in an oven at 70 °C for 24 h (Fig. 1, Step 1) (Maleky et al., 2022; Amiri Fard et al., 2023).

2.2.2. Fe_3O_4@MC/MWCNT-CuO

Following the synthesis of the Fe_3O_4@MC/MWCNT composite, the addition of copper oxide (CuO) was carried out at a 1:1 ratio by microwave-assisted co-precipitation technique. Initially, 3 g of $CuNO_3{\cdot}3H_2O$ were dissolved in 100 mL of distilled water, after which 1 g of Fe_3O_4@MC/MWCNT was introduced into the solution. Subsequently, the pH of the mixture was adjusted to 10–11 using a 0.1 M NaOH solution. The resulting mixture was subjected to microwave irradiation twice for 5 min each, with a power of 600 W. Following irradiation, the black precipitate of Fe_3O_4@MC/MWCNT-CuO was isolated using a magnet and washed several times with distilled water until reaching a neutral pH (Fig. 1, Step 2) (Farghali et al., 2013).

2.2.3. Fe_3O_4@MC/MWCNT-CuO/Ag

To synthesize Ag^0 on the Fe_3O_4@MC/MWCNT-CuO composite, we employed a hybrid reduction approach employing NH_4OH and UV irradiation simultaneously to enhance the efficiency of Ag^0 formation. A silver to Fe_3O_4@MC/MWCNT-CuO ratio of 1:5 was utilized for the silver synthesis on the ferrite component. Initially, 0.2 g of $AgNO_3$ was dissolved in 100 mL of distilled water, followed by adding 1 g of Fe_3O_4@MC/MWCNT-CuO to the solution. Subsequently, NH_4OH was slowly added dropwise until the pH reached 11, and the mixture was stirred for 2 h. It was then exposed to UV light with a power of 15 W for 12 h to facilitate the reduction of Ag^+ to Ag^0. Finally, the black precipitate of Fe_3O_4@MC/MWCNT-CuO/Ag was collected using a magnet and washed multiple times with distilled water to achieve a neutral pH (Fig. 1, Step 3) (Moreira et al., 2023; Jaafar et al., 2015).

2.3. Characterization of nanocomposite

A comprehensive array of techniques, including X-ray diffraction (XRD), field emission scanning electron microscopy (FESEM), vibrating sample magnetometry (VSM), energy-dispersive X-ray spectroscopy (EDS) & mapping, Brunauer-Emmett-Teller (BET) analysis, Fourier-transform infrared spectroscopy (FTIR), diffuse reflectance spectroscopy (DRS), photoluminescence spectroscopy (PL), and thermogravimetric analysis (TGA), were employed to scrutinize the structural properties of the nano-composite meticulously. Structural integrity and phase composition were assessed using FESEM (TESCAN MIRA III) and XRD (PHILIPS PW1730). EDS-mapping (TESCAN MIRA II with SAMX Detector) was employed to ascertain the kinds, surface distribution, and percentages of elemental weight. FTIR (Thermo, AVATAR) made it easier to identify functional groups and analyze chemical bonds. The specific surface area was determined using BET analysis (BELSORP Mini II), while the magnetic characteristics were evaluated using VSM (MDKB). Thermal stability was assessed using TGA (SDT, Q600), and bandgap changes in the nano-composite structure by water as a dispersant were clarified using DRS (S_4100 SCINCO). PL (Varian) analysis for determining the optical absorption characterization of nanocomposite was utilized by dispersion with water. After the nanocomposite had undergone thorough characterization, monoethylene glycol (MEG) was used to assess its photo- and sono-catalytic and adsorption capabilities and measured by HPLC through the Schotten-Baumann method (Martínez, 2020).

2.4. Batch experiments

Batch studies were carried out to assess the effectiveness of removing MEG from aqueous solutions with a synthesized Fe_3O_4@MC/MWCNT-CuO/Ag nanocomposite. Adsorption, photocatalysis, and sonocatalytic degradation were all investigated with triple repetition. The initial MEG

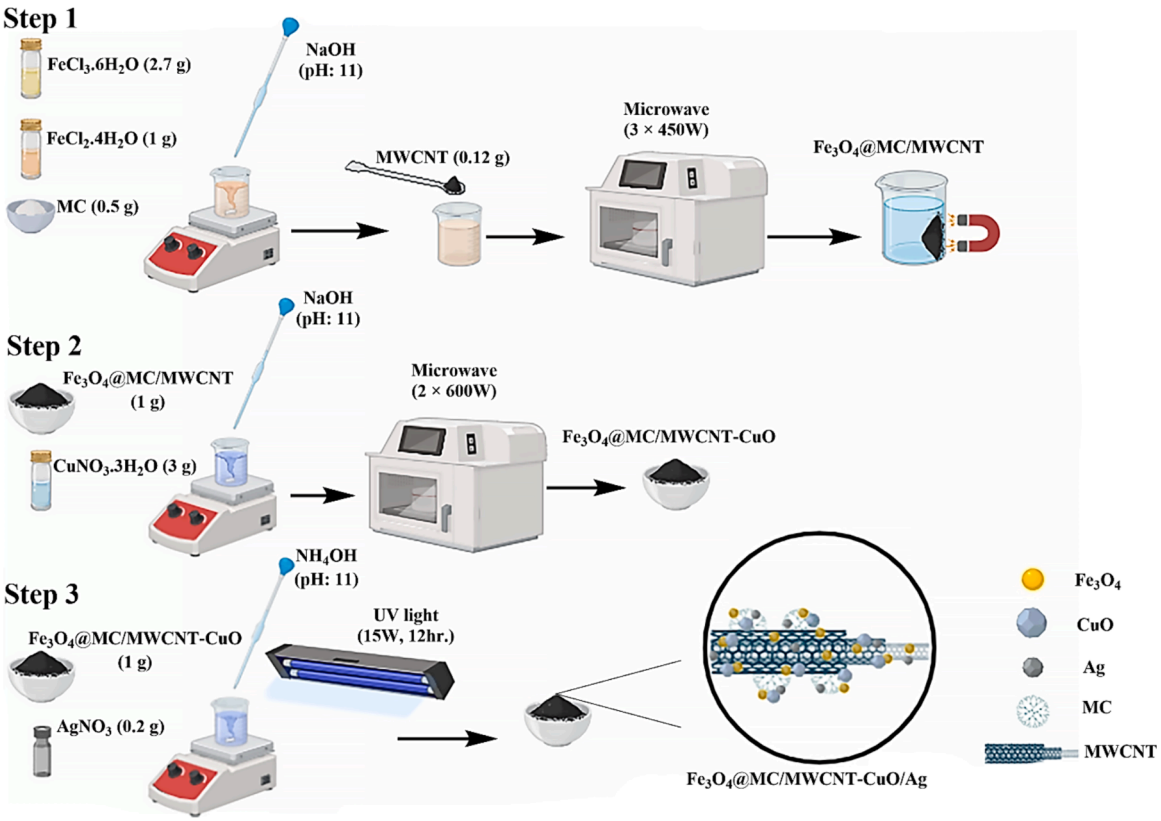

Fig. 1. Synthesis procedure of Fe_3O_4@MC/MWCNT-CuO/Ag.

concentration was 15 mg/L, and the nanocomposite dosage was 0.8 g/L for the adsorption studies. Experiments were conducted at ambient temperature with the solution at pH 6. The nanocomposite and MEG molecules were continually agitated to maintain optimal interaction. The catalytic studies were performed under identical circumstances but with a nanocomposite dosage of 0.5 g/L. The initial concentration of MEG was fixed at 15 mg/L, while the solution pH was maintained at 6, and the temperature was held at room temperature. The procedure included continuous agitation to augment the interplay between the catalyst and MEG. The removal efficiency (*RE*) of MEG was determined using the following equation (Eq. 1):

$$RE = \frac{C_0 - C_t}{C_0} \times 100 \quad (1)$$

Where C_0 represents the starting concentration of MEG, whereas C_t represents the concentration of MEG at a certain time (Rajabi et al., 2024).

3. Results and discussion

3.1. Specification and characterization of Fe_3O_4@MC/MWCNT-CuO/Ag

3.1.1. FESEM

The FESEM analysis of Fe_3O_4@MC/MWCNT-CuO/Ag nanocomposite reveals several key structural features indicative of its morphology, elemental composition, and size distribution (Fig. 2). Notably, the least agglomeration indicates uniform dispersion and excellent interfacial interaction between the constituent materials. The

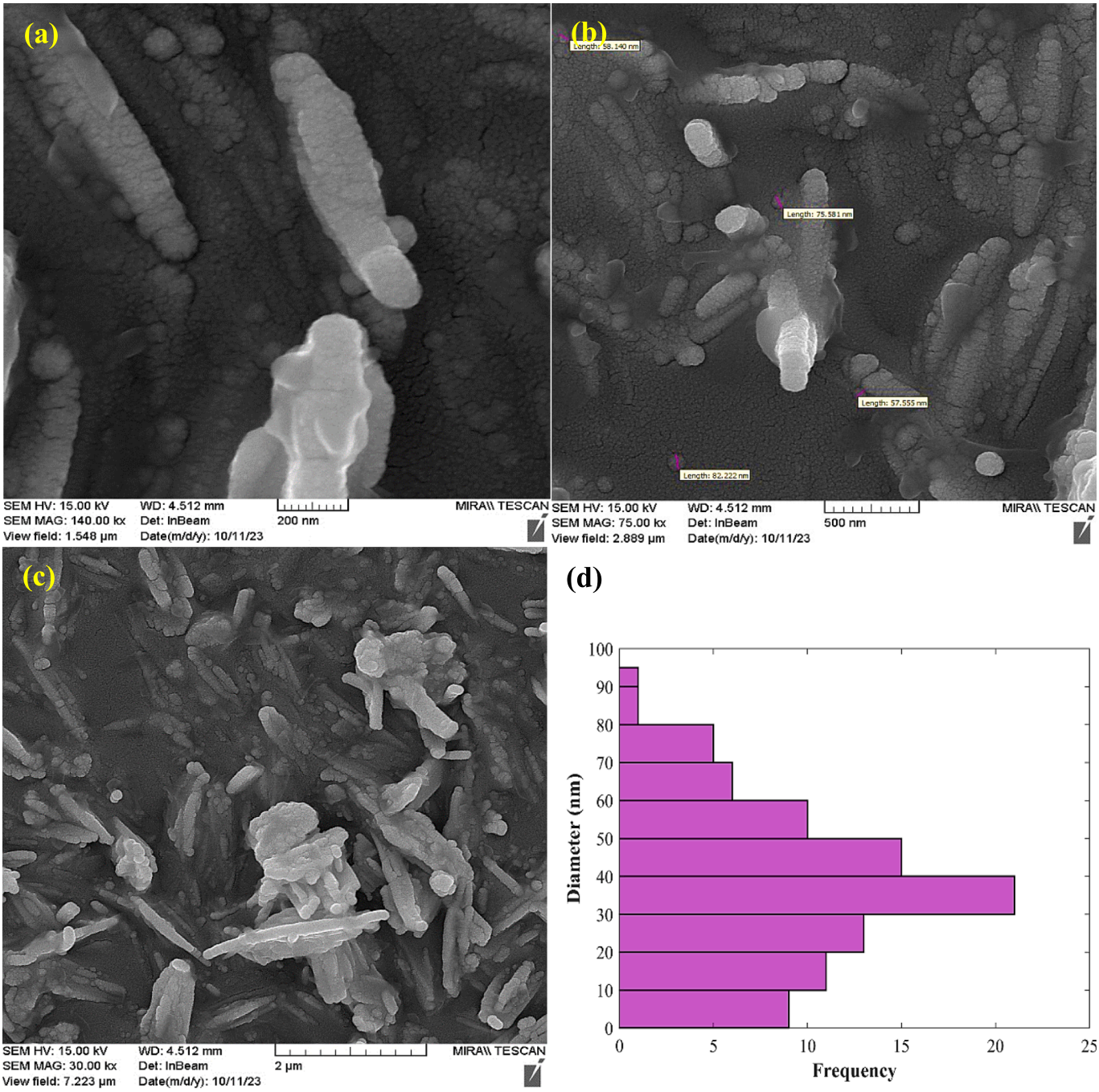

Fig. 2. FESEM images of nanocomposite (a-c) and size distribution histogram (d).

presence of well-doped CuO and Ag on the Fe_3O_4@MC/MWCNT matrix is evident from the distinct and evenly distributed nanoparticles observed under FESEM analysis. The CuO and Ag nanoparticles appear to be uniformly distributed throughout the nanocomposite, suggesting successful incorporation and uniform coverage on the Fe_3O_4@MC/MWCNT substrate. Furthermore, the observed dominant size distribution of nanoparticles ranging from 30 to 40 nm indicates the uniformity of the particle size within the nanocomposite. Nano-scale particles offer increased surface area, enhancing their efficacy in photo- and sono-absorption processes for impurity removal (Kumar et al., 2015). The absence of agglomeration, coupled with the well-doped CuO and Ag nanoparticles, suggests effective synthesis and fabrication techniques employed during the preparation of the Fe_3O_4@MC/MWCNT-CuO/Ag nanocomposite. The uniform distribution and appropriate sizing of nanoparticles are crucial for optimizing the performance and functionality of the material in various applications (Margan and Haghighi, 2018).

3.1.2. FTIR

The FTIR analysis of CuO nanoparticles revealed characteristic wavenumbers. At 503 and 611 cm^{-1}, the observed peaks indicate the stretching vibration of the Cu–O bond within the CuO lattice, confirming the formation of CuO nanoparticles, a hallmark of metal oxide compounds. Peaks detected at 1382 and 3430 cm^{-1} correspond to the stretching vibration of the O–H bond, suggesting the presence of hydroxyl groups or adsorbed moisture and water on the nanoparticle surface (Fig. 3) (Soleimani and Moghaddami, 2018).

The FTIR analysis of multi-walled carbon nanotubes presented characteristic wavenumbers. The peak observed at 1560 cm^{-1} typically corresponds to the stretching vibration of the C–C bonds in the carbon nanotube structure, indicating the presence of sp^2-hybridized carbon atoms within the nanotube lattice. This peak is consistent with the characteristic structure of carbon nanotubes. The peak detected at 3430 cm^{-1} is associated with the stretching vibration of the O–H bond, suggesting the presence of hydroxyl groups or adsorbed moisture and water on the surface of the MWCNTs. This peak is indicative of surface functional groups or interactions with water molecules, which are common in nanomaterials due to their high surface area and reactivity (Fig. 3) (Kabel et al., 2016).

The FTIR analysis of methylcellulose was conducted to elucidate its molecular composition and structural characteristics. Several prominent wavenumbers were observed, each corresponding to specific vibrational modes indicative of distinct chemical functionalities within the methylcellulose molecule. Firstly, the peak detected at 3461 cm^{-1} signifies the stretching vibration of O–H bonds, suggesting the presence of hydroxyl groups within the methylcellulose structure. This observation aligns with the hydrophilic nature of cellulose derivatives. Additionally, the peak observed at 2931 cm^{-1} corresponds to the stretching vibration of C–H bonds, particularly associated with methyl groups ($–CH_3$) present in the methylcellulose molecule. The peak at 1644 cm^{-1} indicates the stretching vibration of C=O bonds, characteristic of carbonyl groups (C=O) typically found in the cellulose backbone of methylcellulose (Nasiri et al., 2021; Rodrigues Filho et al., 2007). Furthermore, peaks at 1458 cm^{-1}, 1378 cm^{-1}, and 1315 cm^{-1} are attributed to bending vibrations of C–H bonds, likely arising from methyl groups and CH_2 groups within the cellulose structure. The peak observed at 1067 cm^{-1} corresponds to the stretching vibration of C-O-C bonds, indicative of ether linkages present in the methylcellulose molecule. Moreover, the peak at 946 cm^{-1} is associated with the bending vibration of C–H bonds in methyl groups ($–CH_3$), further supporting the presence of methyl substituents. Finally, peaks at 569 cm^{-1} and 473 cm^{-1} represent out-of-plane bending vibrations of C–H bonds in methyl groups, providing additional confirmation of the methyl substituents within the methylcellulose structure (Fig. 3) (Nasiri et al., 2022; Sekiguchi et al., 2003).

The FTIR analysis of Fe_3O_4@MC/MWCNT-CuO/Ag nanocomposite provides valuable insights into its molecular composition and structural characteristics, which determined each corresponding to specific vibrational modes indicative of distinct chemical functionalities within the nanocomposite. The peak detected at 3413 cm^{-1} signifies the stretching vibration of O–H bonds, suggesting the presence of hydroxyl groups within the nanocomposite structure. This observation aligns with the presence of hydrophilic components such as MC and metal oxides. The peak observed at 2033 cm^{-1} is attributed to the stretching vibration of C=C bonds, characteristic of carbon double bonds, which could be associated with the presence of MWCNTs within the composite. Furthermore, peaks at 1616 cm^{-1}, 1452 cm^{-1}, and 1400 cm^{-1} are associated with the stretching vibrations of C=O bonds, suggesting the presence of carbonyl groups within the nanocomposite structure, possibly originating from the MC component. The peak observed at 1163 cm^{-1} corresponds to the stretching vibration of C-O bonds, indicative of ether linkages presented in the composite structure, likely originating from MC. The incorporation of functional groups within the methylcellulose structure and their verification within the composite structure promote electrostatic interactions at the composite surface with the pollutant, thereby enhancing catalytic performance during photo- and sono-processes, as well as improving adsorption efficiency.

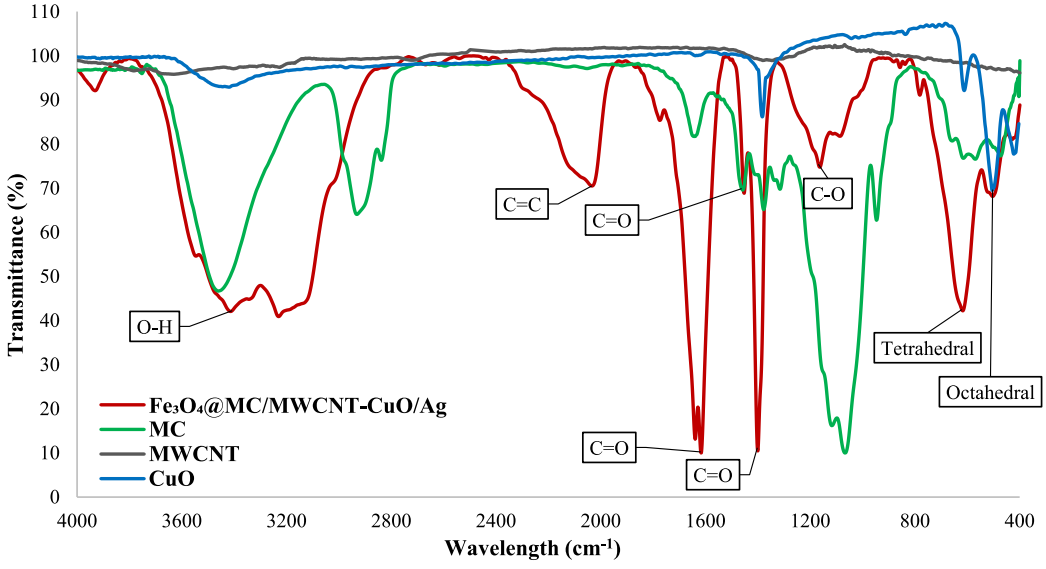

Fig. 3. FTIR of nanocomposite (Red), Methylcellulose (Green), CuO (Blue), and MWCNT (Black).

Moreover, peaks at 617 cm^{-1} for tetrahedral structure and 503 cm^{-1} octahedral structure represent vibrations associated with metal–oxygen (M−O) bonds, characteristic of metal oxides such as Fe_3O_4 and CuO present in the nanocomposite (Fig. 3) (Nasiri et al., 2022; Nasiri et al., 2024).

3.1.3. XRD

The nanocomposite crystallographic properties were investigated through XRD analysis, utilizing a copper (Cu) X-ray source with a wavelength of 1.5406 Å for the Kα1 line (Fig. 4). Utilizing the X'Pert HighScore Plus software version 3.05, we determined the *hkl* values and crystallite size using the Miller indices equations (Eq. 2) (Elahi and Gull, 2024), the Debye-Sherrer equations (Eq. 3) (Hamidi and Karimi Zarchi, 2018), and Williamson-Hall model (Eq. 4), respectively.

$$2d_{hkl}.sin\theta = n\lambda \;\&\; \frac{1}{d_{hkl}^2} = \frac{h^2+k^2+l^2}{a^2} \tag{2}$$

$$D = K.\lambda \Big/ \beta.cos\theta \;\&\; \beta = \frac{\frac{FWHM}{2} \times \pi}{180} \tag{3}$$

$$\beta.cos\theta = K.\lambda/D + 4\epsilon \sin(\theta) \tag{4}$$

In the equations, d_{hkl} represents the spacing between crystal planes with Miller indices *hkl*, θ stands for the diffraction angle, and *n* denotes the order of diffraction, typically 1 for XRD analysis. The *a* parameter signifies the lattice parameter. *K* denotes the Sherrer constant, usually assigned a value of 0.9. λ represents the X-ray wavelength, determined by the Cu Kα1 source, approximately 1.5418 Å. Finally, β indicates the angular line width at half maximum intensity, calculated using the full width at half maximum (*FWHM*) value. The presence of Microstrain is indicated by ϵ, and the slope of the line corresponds to 4ϵ, which provides information on the strain.

The XRD pattern unveiled distinct diffraction peaks corresponding to various crystalline phases present in the nanocomposite. The presence of the Fe_3O_4 phase was confirmed by observing diffraction peaks at 2θ values of 30.4°, 35.8°, 57.8°, 63.5°, and 75.2°, matched with *hkl* of (022), (113), (115), (044), and (335), respectively. These peaks align well with standard reference data for Fe_3O_4, affirming the existence of magnetite in the nano-composite (Jonak and Borah, 2021).

Likewise, the CuO phase was identified from diffraction peaks observed at 2θ values of 32.8°, 35.8°, 39.1°, 46.6°, 49.1°, 53.9°, 58.7°, 62.0°, 66.7°, 68.6°, 72.9°, and 75.6°, with corresponding *hkl* of (110), (002), (111), (11–2), (20–2), (020), (202), (11–3), (31–1), (220), (311), and (004). The consistency of these peaks with typical copper oxide patterns confirmed the presence of CuO in the nanocomposite (Singh et al., 2022).

Additionally, diffraction peaks at 2θ values of 37.2°, 43.3°, 62.9°, 75.6°, and 79.6°, corresponding to *hkl* of (111), (002), (022), (113), and (222), respectively, indicated the presence of Ag nanoparticles in the

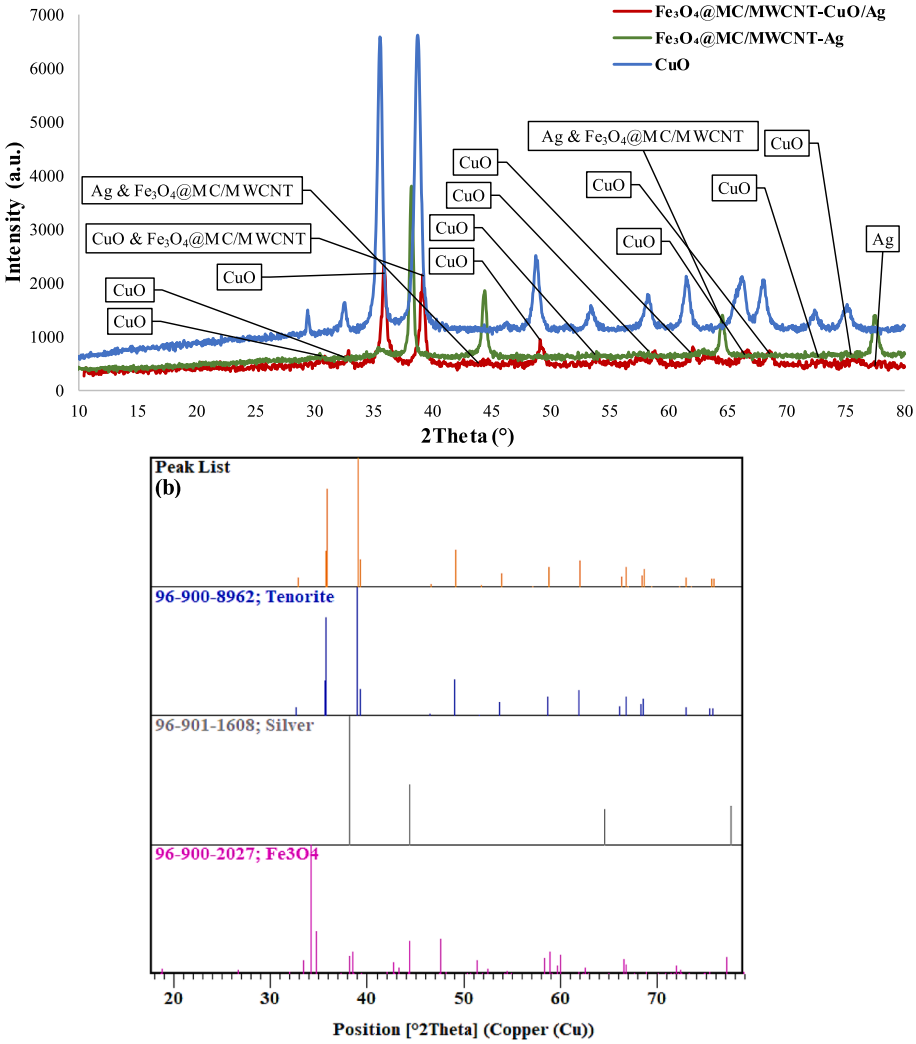

Fig. 4. XRD of the final nanocomposite, Fe_3O_4@MC/MWCNT-Ag, and CuO (a) and phase pattern identification (b).

nano-composite, aligning closely with reference data for silver (Kasina et al., 2024). The Debye-Scherrer model determined that the average size of the crystallites was 8.67 nm. On the other hand, the Williamson-Hall model, which considered both the broadening of the XRD peaks caused by the size of the crystallites and the distortion in their structure, yielded a slightly larger crystallite size of 11.52 nm and a microstrain value of 0.0027. The difference between the two models highlights the impact of lattice strain on the widening of peaks. The Williamson-Hall model successfully distinguishes this strain-induced broadening from the broadening caused by particle size, leading to a more thorough comprehension of the structural properties of the nanocomposite. This small crystallite size suggests the formation of fine-grained structures in the nanocomposite, which could enhance the surface area and reactivity, making it promising for various applications. Furthermore, the nanocomposite has maintained its crystalline structure even after being composited with MWCNT, which inherently possesses an amorphous nature.

3.1.4. EDS & mapping

EDS analysis of the Fe_3O_4@MC/MWCNT-CuO/Ag nanocomposite reveals its chemical composition and elemental mapping validates its uniform distribution (Fig. 5). The predicted elemental percentages of Cu (40.09 %), O (31.93 %), C (14.87 %), Fe (8.81 %), and Ag (1.02 %) inside the nanocomposite were disclosed by the EDS data. Given the

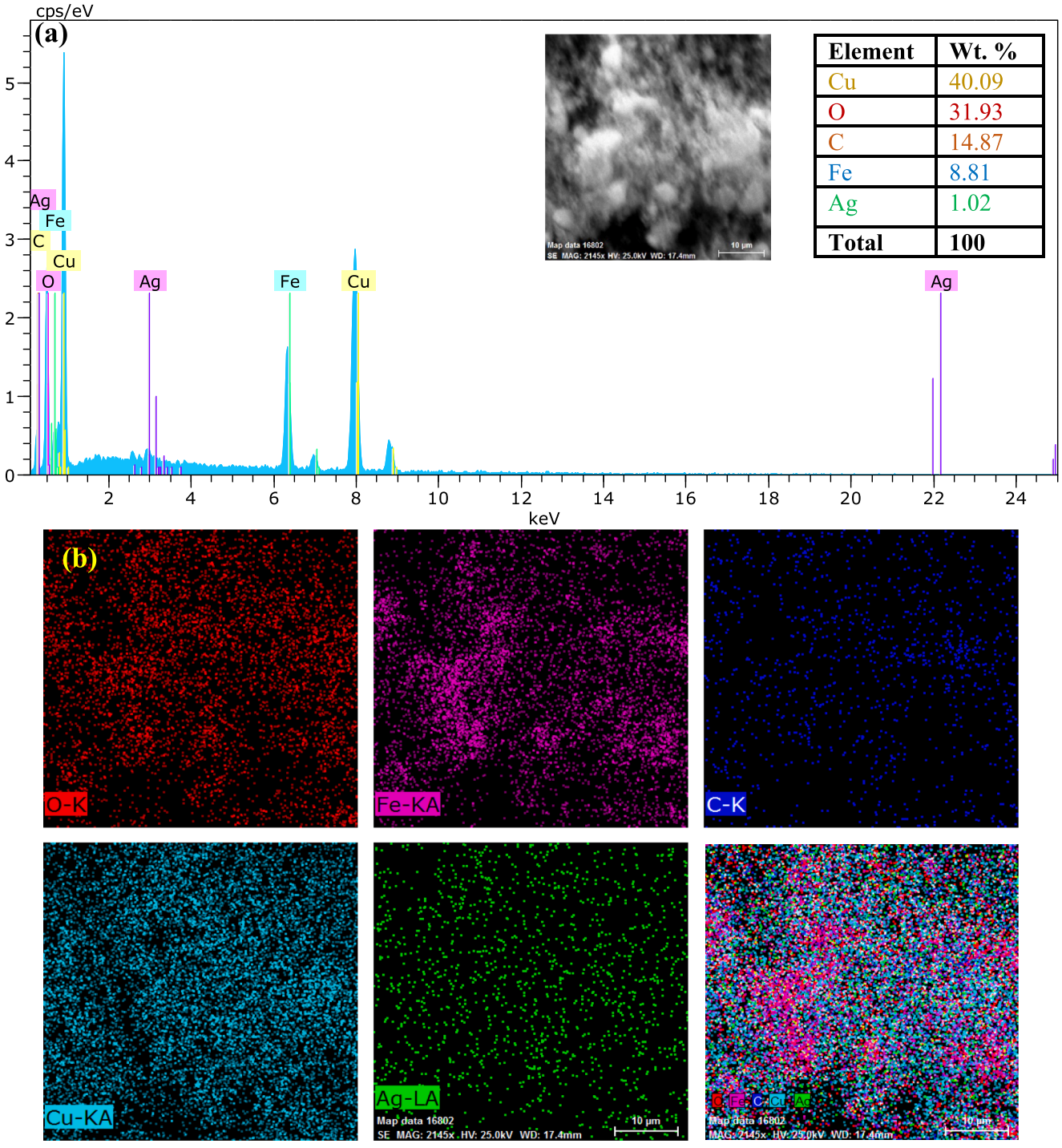

Fig. 5. EDS (a) and Mapping (b) of nanocomposite.

synthesis process and precursor materials, the predicted composition was quite congruent with these results. The effective integration of CuO was shown by the predominance of Cu and O, and the existence of Fe_3O_4 was validated by the Fe content. Furthermore, the presence of silver, while in reduced amounts, verified the effective incorporation of silver nanoparticles. The analytical mapping study showed that all the elements making up the nanocomposite were distributed evenly and uniformly. This supported the previous results. There was a high degree of consistency across all elemental maps, showing that all elements were present in the sample and that they were well-integrated into the matrix.

3.1.5. VSM

The VSM analysis offers insights into the magnetic properties of the Fe_3O_4@MC/MWCNT-CuO/Ag nanocomposite. Three distinct components of the nanocomposite were evaluated including Fe_3O_4@MC/MWCNT, Fe_3O_4@MC/MWCNT-CuO, and Fe_3O_4@MC/MWCNT-CuO/Ag. For Fe_3O_4@MC/MWCNT, the saturation magnetization (Ms) was determined to be 12.96 emu/g, with a remanent magnetization (Mr) of 0.35 emu/g and a coercive force (Hc) of 50 Oe. Subsequent incorporation of CuO into the nanocomposite resulted in a reduction in Ms to 10.45 emu/g and Mr to 0.22 emu/g, while Hc remained constant at 50 Oe. Further addition of Ag led to a decrease in Ms to 9.33 emu/g and an increase in Mr to 0.29 emu/g, with Hc maintaining its value at 50 Oe (Fig. 6). The decline in Ms across the nanocomposite series suggests that the introduction of CuO and Ag nanoparticles leads to a diminishing overall magnetic response. This phenomenon can be attributed to the diamagnetic or paramagnetic nature of CuO and Ag, which counteracts the ferromagnetic behavior of Fe_3O_4. Remarkably, Hc remained consistent throughout the series, indicating that the coercivity of the nanocomposite was unaffected by the inclusion of CuO and Ag. This implies that the magnetic field required to demagnetize the nanocomposite remains unchanged despite compositional modifications. The magnetic nature of the composite enables effortless and rapid separation from the reaction medium, facilitating its recovery and reuse in subsequent cycles. This property not only prevents secondary environmental contamination but also reduces operational costs by minimizing catalyst consumption (Yeganeh-Faal and Kadkhodaei, 2022; Kianfar and Arayesh, 2020).

3.1.6. TGA

The TGA of the Fe_3O_4@MC/MWCNT-CuO/Ag nanocomposite reveals crucial insights into its thermal stability and decomposition behavior. The analysis indicates that the nanocomposite experiences weight loss at various temperature intervals, signifying the minimal degradation and decomposition of its constituent components. At 100 °C, the nanocomposite exhibits a weight loss of 1.65 %, indicating the removal of adsorbed moisture and volatile components. This initial weight loss is typical for materials with hygroscopic properties and suggests the presence of residual moisture. Between 100 °C and 126 °C, the nanocomposite undergoes further degradation, with an additional weight loss of 0.06 %. This degradation may be attributed to the decomposition of organic moieties present in the matrix, such as the methylcellulose and multi-walled carbon nanotubes. Interestingly, beyond 126 °C, the nanocomposite experiences a slight increase in weight, reaching 99.22 % at 600 °C (Fig. 7). This phenomenon suggests a potential phase transformation or chemical reaction occurring within the nanocomposite structure and can be attributed to the oxidation of carbonaceous species and metallic elements. The maximal weight loss observed (0.78 %, 0.025 mg) indicates a relatively stable composition under elevated temperatures. The excellent thermal stability of the catalyst ensures that any temperature increase during the pollutant removal process will not compromise or degrade its structure.

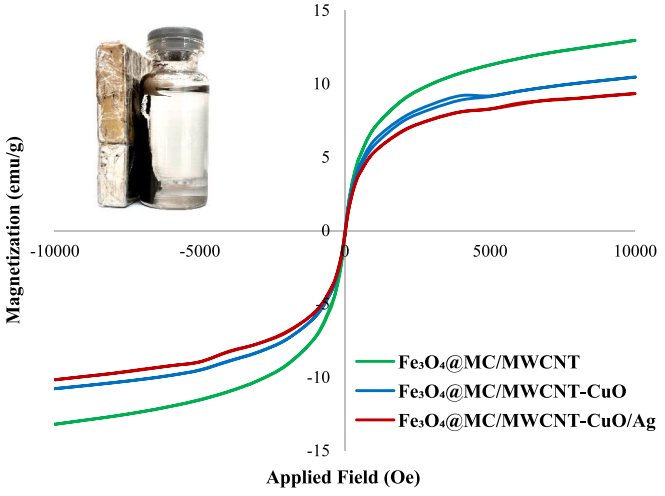

Fig. 6. VSM of final nanocomposite, Fe_3O_4@MC/MWCNT, and Fe_3O_4@MC/MWCNT-CuO.

3.1.7. BET

The BET analysis of the Fe_3O_4@MC/MWCNT-CuO/Ag nanocomposite provides valuable information about its surface area, pore characteristics, and adsorption behavior (Fig. 8). The analysis was conducted following degassing at 120 °C for N_2, ensuring the removal of any adsorbed gases or impurities from the nanocomposite surface. The standard volume of the nanocomposite, measured at 9.779 cm^3, indicates the amount of N_2 gas adsorbed during the BET analysis. Conversely, the dead volume, recorded at 16.521 cm^3, represents the volume of gas not adsorbed due to inaccessible pores or non-porous regions within the nanocomposite structure. The calculated specific surface area ($a_{s,BET}$) of 67.661 m^2/g reflects the extent of accessible surface area available for adsorption, highlighting the porous nature of the nanocomposite. This large surface area is attributed to the presence of mesopores and micropores within the nanocomposite matrix, facilitating enhanced adsorption interactions (Nasiri et al., 2022). In photolytic processes, enhancing the specific surface area of the catalyst promotes greater interaction between the catalyst surface and photons emitted by the UV lamp. This interaction fosters increased generation of active free radicals and electron/hole pairs, ultimately boosting the process efficiency (Wang et al., 2016). The extensive surface area of nanoparticles in sonocatalytic processes significantly boosts catalytic efficiency by providing more active sites, facilitating better mass transfer of reactants, promoting effective ultrasound absorption, facilitating the generation of electron/hole pairs, and leveraging synergistic effects within composite materials (Zhu et al., 2013). The total pore volume, determined to be 0.194 cm^3/g, quantifies the cumulative volume of all pores within the nanocomposite structure. The mean pore diameter of 11.495 nm suggests the presence of mesopores, which are conducive to efficient mass transport and adsorption processes. The pore size distribution analysis reveals a peak pore diameter ($r_{p,peak}$) of 1.85 nm, indicating the predominant pore size within the nanocomposite. Additionally, the calculated specific surface area (a_p) of 78.342 m^2/g corroborates the BET-derived surface area, further confirming the porous architecture of the nanocomposite. Overall, the BET analysis underscores the porous nature and high surface area of the Fe_3O_4@MC/MWCNT-CuO/Ag nanocomposite, highlighting its potential for various applications such as adsorption, catalysis, and sensing.

The BET results revealed a characteristic Type IV hysteresis loop in the adsorption and desorption plot (Fig. 8a), indicating the presence of mesoporous or microporous structures within the material. This type of loop is commonly observed in materials with complex pore networks. During the adsorption process, the adsorption branch displayed a gradual increase in the amount of adsorbate uptake. This initial rise suggests the formation of a monolayer of adsorbate molecules on the surface of the material. As the adsorption continued, the uptake eventually reached a plateau, indicating saturation of the monolayer

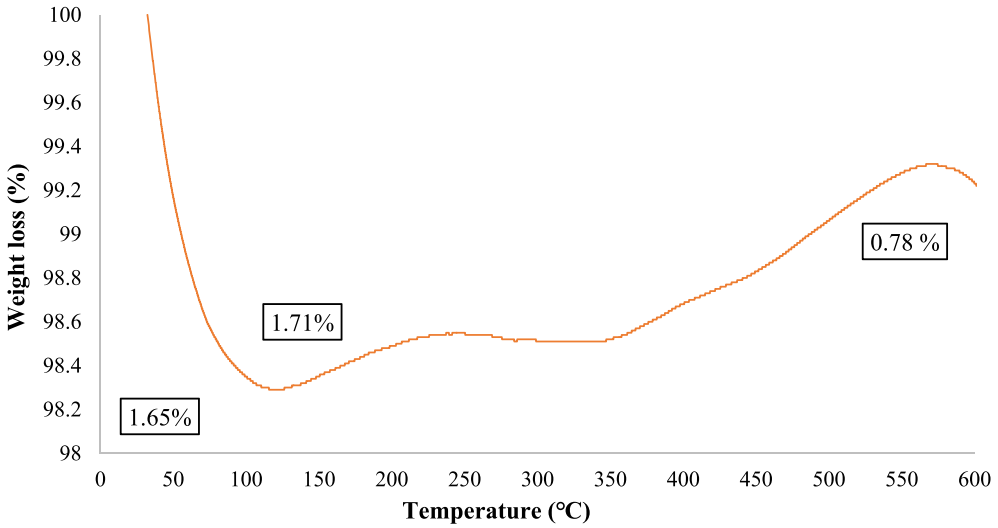

Fig. 7. TGA of nanocomposite.

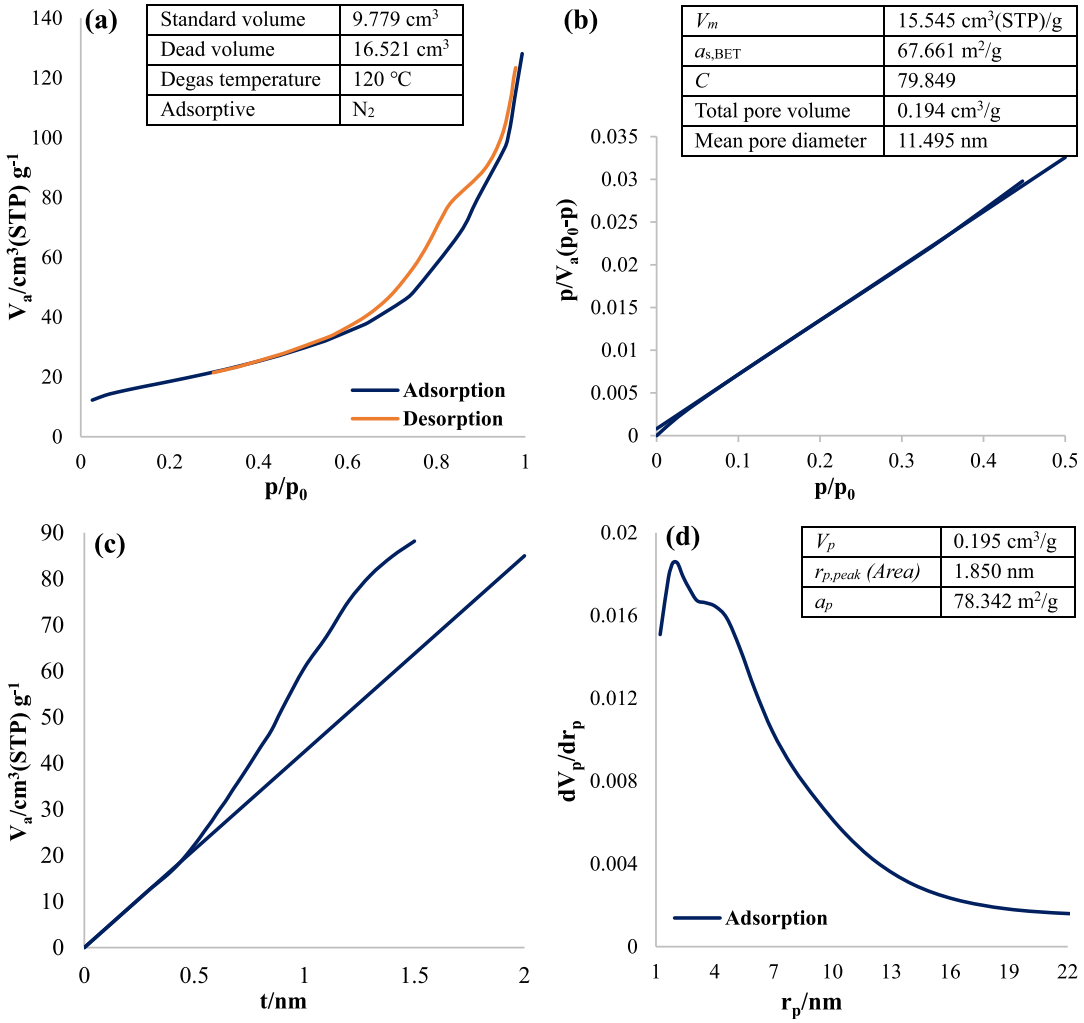

Fig. 8. Adsorption/desorption (a), BET plot (b), t plot (c), and BJH plot (d) of nanocomposite.

adsorption. Conversely, during the desorption process, the desorption branch exhibited a gradual decrease in the amount of adsorbate released from the material. This gradual decline implies the removal of adsorbate molecules from the surface and the pore network of the material. The desorption process may involve the release of adsorbate molecules from both monolayer and multilayer adsorption sites within the pores (Ariga et al., 2012).

3.1.8. DRS

The DRS analysis revealed valuable insights into the excitation properties of the Fe_3O_4@MC/MWCNT, Fe_3O_4@MC/MWCNT-CuO, and Fe_3O_4@MC/MWCNT-CuO/Ag nanocomposites, particularly in terms of their band-gap energies (Fig. 9). Band-gap energy (E) calculation using the Kubelka-Munk transformation involves the determination of the diffuse reflectance (R) of a material and the subsequent transformation of this data to derive the band-gap energy. The Kubelka-Munk equation, represented as Eq. 5, is employed to convert the reflectance data to a linear absorption coefficient. Here, R denotes the diffuse reflectance of the material, and $F(R)$ is the Kubelka-Munk function. The absorbance (A) can be calculated from $F(R)$ using Eq. 6, allowing for the transformation of reflectance data to absorption data. Subsequently, the photon energy ($h\nu$) corresponding to a given wavelength (λ) is determined using Eq. 7, where h is the constant of the Planck, c is the speed of light, and λ is the wavelength in meters. This provides the energy of the incident photons in electron volts (eV). Finally, the band-gap energy (Eg) is calculated by multiplying the square root of the product of the Kubelka-Munk function and the photon energy, represented as Eq. 8 (Makuła et al., 2018).

$$F(R) = \frac{(1-R)^2}{2R} \tag{5}$$

$$A = 2.303 log 1/F(R) \tag{6}$$

$$h\nu = E = \frac{hc}{\lambda \times 1.6 \times 10^{-19}} \tag{7}$$

$$E_g = (F(R).h\nu)^{0.5} \tag{8}$$

The Fe_3O_4@MC/MWCNT nanocomposite exhibited a peak absorbance of 1.853 at a wavelength of 307 nm, as determined by DRS analysis. The associated band-gap energy was predicted to be 3.34 eV. Fe_3O_4@MC/MWCNT can be useful in photocatalysis and sonocatalysis due to its broadband gap. Findings showed that Fe_3O_4@MC/MWCNT-CuO had a higher maximum absorbance of 1.991 at 316 nm and a much lower band-gap energy of 1.63 eV. The electrical structure of Fe_3O_4@MC/MWCNT matrix has been changed by CuO nanoparticles, reducing band-gap energy and possibly improving photocatalytic and photoelectrochemical characteristics. The DRS analysis of the Fe_3O_4@MC/MWCNT-CuO/Ag nanocomposite exhibited a maximum absorbance of 1.697 at 265 nm. The band-gap energy was further lowered to 1.31 eV, demonstrating that Ag nanoparticles improve the optical and electrical characteristics of the material, especially in photovoltaics and photocatalysis.

The DRS study shows that these nanocomposites gradually reduce their band-gap energy, which may greatly improve their catalytic properties, especially in photocatalysis and sonocatalysis. Lower band-gap energy suggests that the nanocomposite needs less energy to excite electrons from valence to conduction. Photocatalytic processes generate electron-hole pairs from photon absorption with energy equivalent to or higher than the band gap, making this beneficial. These charge carriers may then degrade organic contaminants or activate catalytic sites through redox processes (Hassani et al., 2017). A smaller band gap might help the nanocomposite absorb ultrasound energy and improve electron transfer in sonocatalysis, where ultrasonic vibrations cause cavitation and create reactive species like hydroxyl radicals. This improved ultrasound absorption efficiency may boost sonocatalytic degradation events, making the nanocomposite more effective in

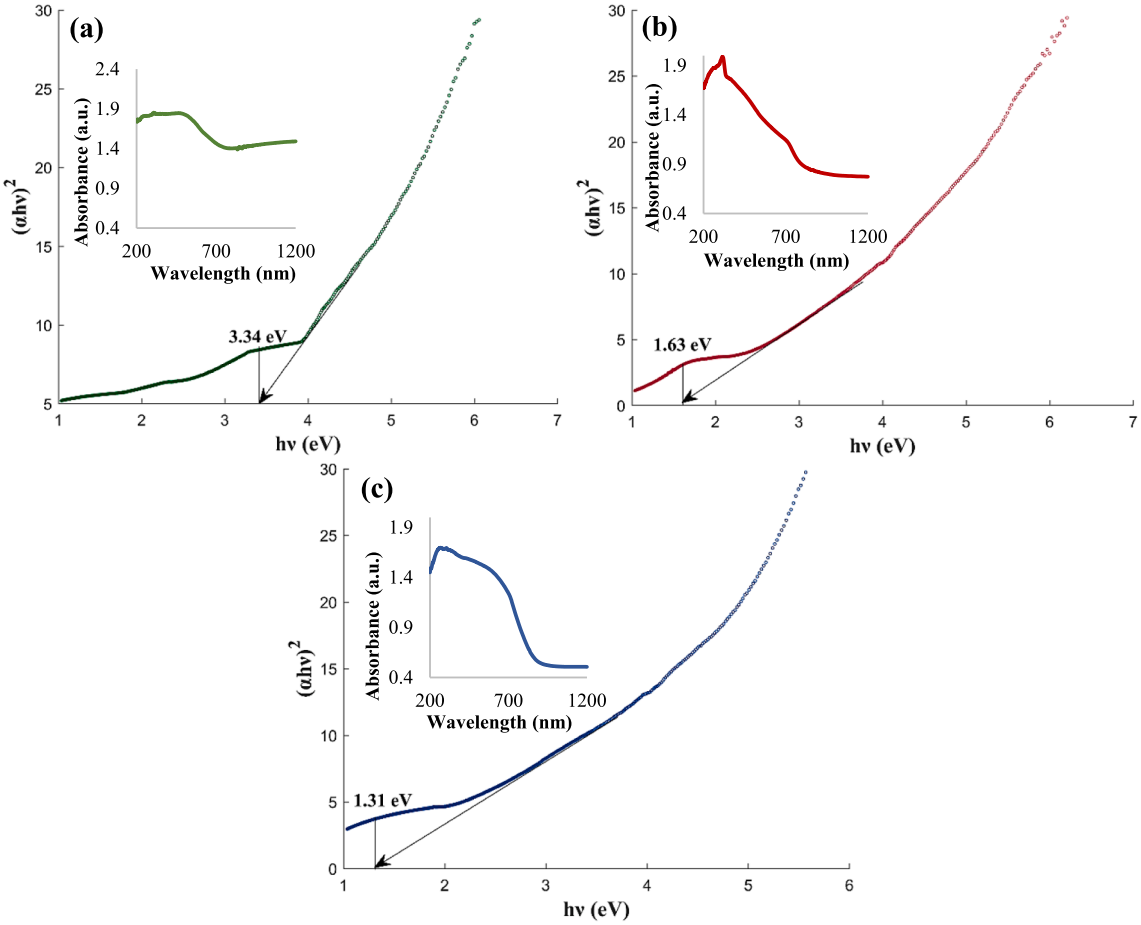

Fig. 9. DRS and bandgap of Fe_3O_4@MC/MWCNT (a), Fe_3O_4@MC/MWCNT-CuO (b), and nanocomposite (c).

environmental cleanup (Khataee et al., 2018).

3.1.9. PL

PL analysis was conducted on Fe_3O_4@MC/MWCNT, Fe_3O_4@MC/MWCNT-CuO, and Fe_3O_4@MC/MWCNT-CuO/Ag nanocomposites with an excitation wavelength of 300 nm (Fig. 10). The PL spectra revealed distinct emission characteristics for each material. In Fe_3O_4@MC/MWCNT, the maximum observed wavelength in the PL spectrum was 398 nm (3.11 eV). For Fe_3O_4@MC/MWCNT-CuO, the PL spectrum exhibited a maximum observed wavelength at 371 nm (3.28 eV). In Fe_3O_4@MC/MWCNT-CuO/Ag, the PL spectrum showed a shift towards longer wavelengths, with a maximum observed wavelength of 409 nm (3.03 eV). These observed wavelengths correspond to the peak emission wavelengths for each nanocomposite under the specified excitation conditions. The differences in the observed wavelengths among the materials suggest variations in their optical properties and electronic band structures. These variations may arise from differences in composition, structure, surface properties, and interactions between components such as CuO and Ag nanoparticles.

Incorporating Ag and CuO nanoparticles into the Fe_3O_4@MC/MWCNT nanocomposite offers several advantages, as revealed by PL analysis. Firstly, the PL analysis showed a shift towards visible wavelengths, low frequency, and low excitation energy in the presence of CuO and Ag nanoparticles, indicating modifications in the electronic band structure and optical properties of the nanocomposite. This suggests that Ag and CuO nanoparticles contribute to the alteration of electronic transitions and energy levels within the nanocomposite. The presence of Ag nanoparticles can enhance the PL emission characteristics of the nanocomposite due to their unique optical and catalytic properties. Ag nanoparticles have a strong localized surface plasmon resonance (LSPR) effect, leading to enhanced light absorption and emission properties (Song et al., 2023). Additionally, Ag nanoparticles can act as electron traps, facilitating charge separation and promoting radiative recombination processes, thereby improving PL emission efficiency. Similarly, CuO nanoparticles can also influence the PL emission of the nanocomposite. CuO nanoparticles have been reported to exhibit strong absorption and emission properties in the visible and near-infrared regions of the electromagnetic spectrum. Incorporating CuO nanoparticles into the nanocomposite can introduce additional energy levels and electronic transitions, leading to modifications in the PL emission spectrum (Ansari et al., 2020).

3.2. Adsorption & catalytic performance

3.2.1. Adsorption process

The adsorption process of monoethylene glycol (MEG) at a concentration of 15 mg/L using 0.8 g/L of Fe_3O_4@MC/MWCNT-CuO/Ag nanocomposite demonstrated promising efficiency, with a removal rate of 72 % and adsorption capacity of 13.5 mg/g. This indicates the high affinity of the nanocomposite for MEG molecules in aqueous solutions. The process was conducted under typical conditions, including a normal pH of 6, room temperature, and a contact time of 30 min. The significant adsorption efficiency observed suggests that Fe_3O_4@MC/MWCNT-CuO/Ag nanocomposite possesses excellent adsorption capacity and affinity towards MEG molecules. The presence of CuO and Ag nanoparticles in the nanocomposite likely contributes to enhanced adsorption properties through their interactions with MEG molecules, possibly via chemical bonding or electrostatic interactions. Moreover, the mesoporous structure of the nanocomposite, as indicated by BET analysis, provides a large surface area and numerous active sites for MEG adsorption, facilitating efficient removal from the aqueous phase. Additionally, the magnetic properties of Fe_3O_4 enable easy separation of the nanocomposite from the solution after the adsorption process, making it a practical and reusable adsorbent for MEG removal from water environments. With a pKa value of 14.22 at 25 °C, MEG exists predominantly in its deprotonated form in aqueous solutions with a pH below its pKa (Lewis et al., 2016). In this case, at a solution pH of 6, MEG molecules are largely present in the deprotonated form due to the acidic nature of the solution. The pH_{zpc} of the adsorbent, determined to be 6.2, indicates the pH at which the surface charge of the adsorbent becomes neutral. At a solution pH below the pH_{zpc}, the surface of the adsorbent is positively charged, favoring the adsorption of negatively charged MEG molecules due to electrostatic attraction (Maleky et al., 2022). Given that the solution pH (6) is lower than both the pKa of MEG and the pH_{zpc} of the adsorbent, the adsorption process is facilitated by electrostatic interactions between the negatively charged MEG molecules and the positively charged surface of the adsorbent. This electrostatic attraction enhances the adsorption of MEG onto the surface of the adsorbent (Nasiri et al., 2024; Nasiri et al., 2022).

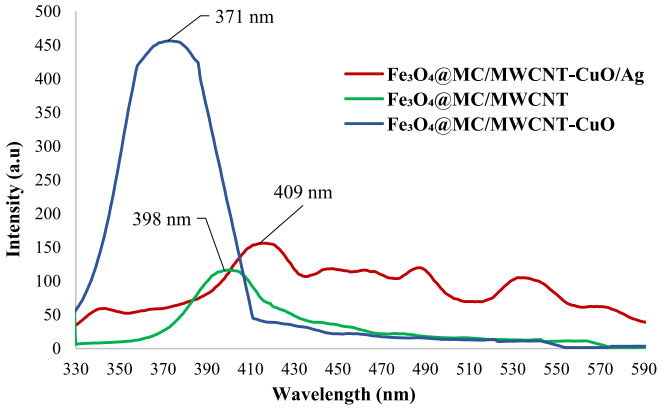

Fig. 10. PL of Fe_3O_4@MC/MWCNT (a), Fe_3O_4@MC/MWCNT-CuO (b), and final nanocomposite (c).

3.2.2. Photocatalytic process

The photocatalytic degradation of MEG by Fe_3O_4@MC/MWCNT-CuO/Ag nanocomposite under normal pH (6), room temperature, MEG concentration of 15 mg/L, catalyst dose of 0.5 g/L, and a reaction time of 20 min resulted in an observed efficiency of 65 %. This process takes advantage of the unique properties of CuO and Ag nanoparticles integrated into the photocatalyst. The photocatalytic degradation process involving Fe_3O_4@MC/MWCNT-CuO/Ag nanocomposite and MEG encompasses a complex interplay of chemical reactions driven by the generation and subsequent reaction of radical species. Upon exposure to light, CuO and Ag nanoparticles embedded in the nanocomposite absorb photons and generate electron-hole pairs. These photoexcited electrons and holes can then migrate to the surface of the catalyst, where they participate in redox reactions with adsorbed species, including MEG molecules. CuO, with its narrow bandgap, efficiently promotes charge carrier generation and separation, facilitating the oxidation of MEG molecules by donating electrons to oxygen molecules or hydroxide ions and oxidizing them to superoxide radicals ($^{\bullet}O_2^-$) or hydroxyl radicals ($^{\bullet}OH$), respectively. Simultaneously, the Ag nanoparticles contribute to the photocatalytic process by enhancing light absorption through surface plasmon resonance effects (Low et al., 2018; Panahi et al., 2023; Karami et al., 2023; Esmaeili et al., 2011). Upon excitation, Ag nanoparticles can directly generate electron-hole pairs or induce local electromagnetic fields, enhancing the absorption of photons by the surrounding catalyst and promoting charge separation. Moreover, Ag nanoparticles possess inherent catalytic properties, promoting the generation of reactive oxygen species (ROS) such as singlet oxygen ($^1O_2$) or hydroxyl radicals ($^{\bullet}OH$) through reactions with adsorbed oxygen molecules or water molecules (Yang et al., 2022; Luo et al., 2021; Salavati-Niasari, 2006; Mahdavi et al., 2022).

The synergy between CuO and Ag nanoparticles within the nanocomposite results in improved photocatalytic activity, with CuO facilitating charge carrier generation and Ag enhancing light absorption and

ROS generation. This synergistic effect manifests in the observed high efficiency of MEG degradation. The presence of these radical species, particularly hydroxyl radicals ($^{\bullet}OH$), plays a crucial role in the degradation of MEG molecules. Hydroxyl radicals are highly reactive and can readily react with organic contaminants like MEG, initiating a cascade of oxidation reactions that ultimately lead to the mineralization of the pollutant into harmless byproducts such as carbon dioxide and water (Asenath-Smith et al., 2020; Karami et al., 2020; Salavati-Niasari et al., 2009; Khojasteh et al., 2017). Furthermore, the unique structure and composition of the nanocomposite facilitate the generation and localization of radical species near the catalyst surface, thereby increasing the likelihood of radical-MEG interactions and enhancing the overall photocatalytic efficiency. The high surface area and porous structure of the nanocomposite provide ample active sites for MEG adsorption and subsequent radical-mediated degradation. In conclusion, the Fe_3O_4@MC/MWCNT-CuO/Ag nanocomposite exhibits exceptional photocatalytic activity towards MEG degradation, driven by the synergistic effects of CuO and Ag nanoparticles. The generation and localization of radical species near the catalyst surface play a pivotal role in initiating and propagating the degradation reactions, highlighting the nanocomposite potential for efficient environmental remediation applications (Mahdavi et al., 2022; Bahnemann et al., 2018; Zinatloo-Ajabshir et al., 2019; Ren et al., 2024). The results of this investigation closely corresponded with the findings of Rajabi et al. (Rajabi et al., 2024), Pourshaban and Nasiri (Pourshaban-Mazandarani and Nasiri, 2024), and Amiri et al. (Gharaghani et al., 2024), providing additional confirmation of the main processes involved in the elimination of organic contaminants.

3.2.3. *Sonocatalytic process*

The sonocatalytic degradation of MEG using Fe_3O_4@MC/MWCNT-CuO/Ag nanocomposite under ultrasound irradiation involves intricate mechanisms influenced by radical generation and the sonoluminescence phenomenon associated with CuO nanoparticles. The observed efficiency of 56 % in the sonocatalytic degradation of MEG highlights the effectiveness of the Fe_3O_4@MC/MWCNT-CuO/Ag nanocomposite under ultrasound irradiation under operational conditions catalyst dose 0.5 g/L, room temperature, MEG concentration of 15 mg/L, reaction time of 5 min, and normal pH of 6. The Fe_3O_4@MC/MWCNT-CuO/Ag nanocomposite acts as a sonocatalyst, enhancing the efficiency of the sonocatalytic degradation process (Fig. 11). The presence of CuO and Ag nanoparticles facilitates the absorption of ultrasound energy and enhances the generation of radical species through mechanisms such as piezoelectric effects and local hot spot formation (Malakootian et al., 2020). Moreover, the high surface area and porous structure of the nanocomposite provide ample sites for the adsorption of MEG molecules, promoting their interaction with radical species generated during cavitation. Copper oxide nanoparticles exhibit the intriguing ability to influence the speed of sound and ultrasonic attenuation coefficient in aqueous media, thereby playing a significant role in enhancing the sonochemical processes for pollutant degradation. When dispersed in water, CuO nanoparticles interact with ultrasound waves, leading to alterations in acoustic properties that contribute to improved efficiency in pollutant removal. One notable effect of CuO nanoparticles is their impact on the speed of sound in water. Due to their unique acoustic characteristics and interaction with ultrasound waves, CuO nanoparticles can modulate the velocity at which sound propagates through the medium. This alteration in the speed of sound facilitates the generation and propagation of acoustic cavitation, a phenomenon crucial for sonochemical reactions. By influencing the speed of sound, CuO nanoparticles contribute to the creation of microbubbles and acoustic hotspots, which enhance the generation of reactive species responsible for pollutant degradation (Perlman et al., 2015).

Additionally, CuO nanoparticles can affect the ultrasonic attenuation coefficient, which measures the rate at which ultrasound waves lose energy as they propagate through a medium. By adsorbing ultrasound waves and promoting acoustic cavitation, CuO nanoparticles contribute to increased energy dissipation and attenuation of ultrasound waves. This heightened attenuation coefficient enhances the intensity of acoustic cavitation and the generation of reactive species, thereby augmenting the efficiency of sonochemical degradation processes (Sarode et al., 2020). Furthermore, studies have indicated that during the momentary collapse of cavitation bubbles, a phenomenon known as “sonoluminescence” occurs. This process involves the emission of light spanning from the ultraviolet to beyond the visible red spectrum, with a peak at 310 nm. The sonoluminescent emission spectrum observed in water is linked to the generation of high-energy species, such as excited hydroxyl radicals, resulting from the molecular fragmentation of compressed gases within the collapsing bubbles (Cao et al., 2012). Unlike black body radiation, which is characteristic of thermal processes, sonoluminescence involves the emission of light energy for a brief duration. While molecular excitation is primarily thermal, the emitted

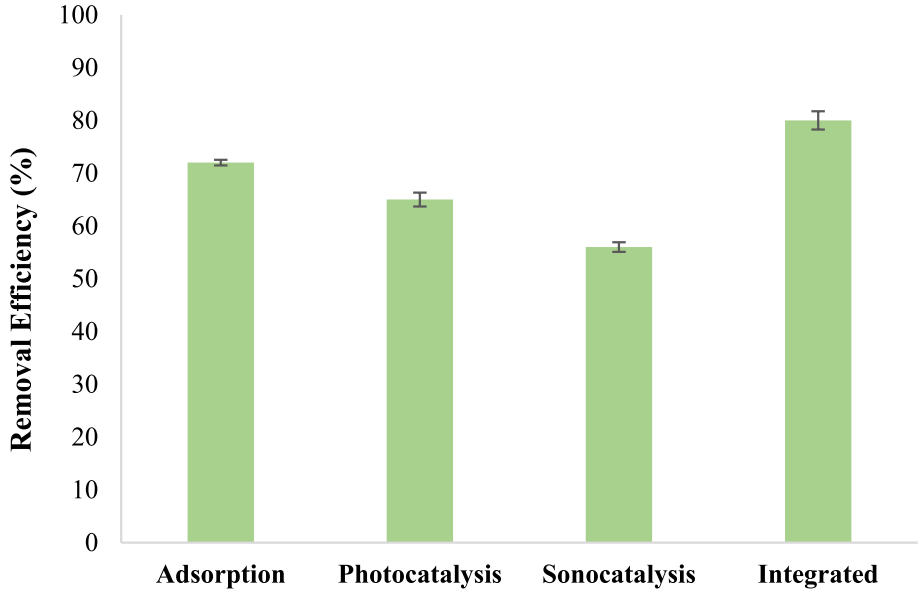

Fig. 11. Removal Efficiency of MEG in different processes (Adsorption: 0.8 g/L of nanocomposite, 15 mg/L of MEG, and pH 6; Photocatalysis and Sonocatalysis: 0.5 g/L of nanocomposite, 15 mg/L of MEG, and pH 6).

radiation may induce photoexcitation of electrons, causing them to be transitioned from the valence band to the conduction band, similar to the mechanism observed in photocatalysis processes (Chauhan et al., 2020). Consistent with previous research by Rajabi et al. (Rajabi et al., 2022), Xu et al. (Xu et al., 2023), and Zhang et al. (Zhang et al., 2023), the findings of this study supported the principal mechanism for organic pollutant removal. The consistency seen in several investigations enhanced the validity of the current findings and verified the efficacy of the proposed nanocomposite system in degrading organic contaminants.

The enhancement factor (EF) was calculated using Equation (9) to assess the synergistic impact of the combined adsorption, photocatalysis, and sonocatalysis systems on MEG removal relative to the impact of each treatment approach separately (Dehvari et al., 2023).

$$EF = \frac{R_{(Adsorption+Photocatalytic+Sonocatalytic)}}{R_{(Adsorption)} + R_{(Photocatalytic)} + R_{(Sonocatalytic)}} \quad (9)$$

Where, the removal efficiencies of MEG for each process are denoted by *R(Adsorption)*, *R(Photocatalytic)*, and *R(Sonocatalytic)*, respectively. For MEG removal, the computed enhancement factor (EF) was higher than 1, indicating a synergistic impact. This result suggests that the total removal efficiency of the integrated system is much greater than the sum of its component operations.

3.3. Chemical and structural stability of nanocomposite

After the catalytic procedure, the XRD analysis of the Fe_3O_4@MC/MWCNT-CuO/Ag nanocomposite showed an augmentation in the intensity of distinctive peaks (Fig. 12). The observed rise in XRD peak intensity after the catalytic procedure suggests an improvement in crystallinity and potential structural changes within the Fe_3O_4@MC/MWCNT-CuO/Ag nanocomposite. This indicates that the catalytic activity has maintained, and maybe enhanced, the organized structure of atoms in the crystal lattice. The high acuity and lucidity of the peaks indicate the durability of the framework of the composite throughout operating circumstances. The distinctive peaks for Fe_3O_4, CuO, and Ag indicate that the constituent components of the nanocomposite are chemically stable without undergoing considerable oxidation, reduction, or other chemical alterations that would modify their crystalline phases (Carta et al., 2009). This stability enables continuous catalytic activity and reduces catalyst deactivation, making the nanocomposite beneficial in long-term applications. The rise in maximum intensity might also indicate a decrease in flaws or imperfections within the crystal lattice, which could increase the number of reactive sites for catalytic activity (Kumar et al., 2013). Following the catalytic process, leaching analysis was performed to assess the chemical stability of the catalyst using an atomic absorption device (AAS, CTA 3000) at wavelengths of 248.3 nm, 324.8 nm, and 328.07 nm to measure the quantities of iron, copper, and silver, respectively. The measured values were 0.42 mg/L of iron, 0.5 mg/L of copper, and 0.11 mg/L of silver. The findings indicate that the catalyst demonstrated exceptional stability throughout the operation in accordance with the World Health Organization (WHO) requirements (Rajabi et al., 2022; Feichtmeier and Leopold, 2014).

4. Conclusion

In this study, the nanocomposite Fe_3O_4@MC/MWCNT-CuO/Ag was successfully synthesized using a hybrid co-precipitation and reduction method under microwave irradiation, leveraging methylcellulose as a natural polysaccharide binder. Structural characterization through FESEM revealed well-dispersed nanoparticles with a size predominantly in the range of 30–40 nm, demonstrating uniformity and least aggregation. Furthermore, the incorporation of CuO and Ag nanoparticles onto the ferrite structure was confirmed, indicating successful doping. FTIR analysis confirmed the integration of methylcellulose within the nanocomposite matrix, while XRD analysis showcased the preserved crystal structure even with the presence of CuO and Ag, with an average crystallite size of 8.67 nm. EDS and mapping analysis affirmed the expected elemental composition and uniform distribution within the nanocomposite structure. VSM analysis demonstrated that adding CuO and Ag nanoparticles did not compromise the magnetic properties of the nanocomposite, enabling easy separation via magnetic means (Ms: 9.33 emu/g). TGA analysis revealed high thermal stability of the nanocomposite up to 600 ℃ (Weight loss: 0.78 %). The BET analysis highlighted the exceptionally high surface area of nanocomposite (67.661 m^2/g), facilitating efficient contact with pollutant molecules. DRS and PL analyses indicated a reduced bandgap of 1.31 eV and enhanced optical absorption in the presence of CuO and Ag nanoparticles. Performance evaluations in adsorption, photocatalytic, and sonocatalytic processes demonstrated removal efficiencies of 72 %, 65 %, and 56 %, respectively. These results underscore the efficacy of nanocomposite in chemical processes for organic pollutant removal, has chemical and structural stability, and present promising ways for advancing nanoparticle-based technologies in environmental remediation applications.

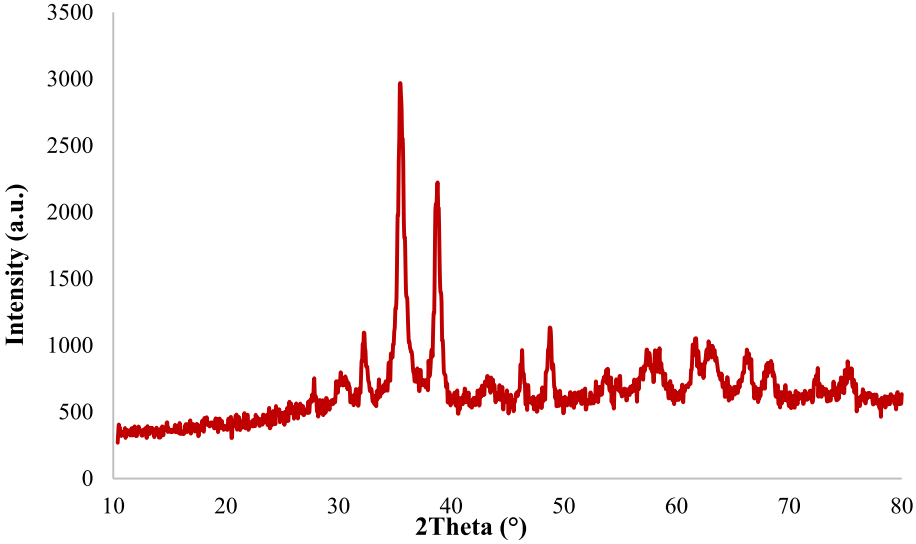

Fig. 12. XRD analysis after the catalytic process and recovery.

CRediT authorship contribution statement

Saeed Rajabi: Writing – original draft, Validation, Supervision, Data curation, Conceptualization. **Hassan Hashemi:** Writing – original draft, Validation, Supervision, Project administration, Methodology, Investigation, Funding acquisition, Data curation, Conceptualization. **Mohammad Reza Samaei:** Writing – original draft, Validation, Project administration, Data curation, Conceptualization. **Alireza Nasiri:** Writing – review & editing, Writing – original draft, Validation, Methodology, Investigation, Data curation, Conceptualization. **Abooalfazl Azhdarpoor:** Writing – original draft, Methodology, Formal analysis, Data curation, Conceptualization. **Saeed Yousefinejad:** Writing – original draft, Validation, Supervision, Data curation, Conceptualization.

Declaration of competing interest

The authors declare that they have no known competing financial interests or personal relationships that could have appeared to influence the work reported in this paper.

Acknowledgments

This paper is extracted from a Ph.D. dissertation conducted within the Department of Environmental Health Engineering at Shiraz University of Medical Sciences, with the registration code of 27865 and the ethics code of IR.SUMS.SCHEANUT.REC.1402.021. Gratitude is extended to the esteemed Vice-Chancellor for Research and Technology and Environmental Health Engineering Research Center of Kerman University of Medical Sciences for their invaluable support and provision of necessary facilities for the successful execution of this study.

References

Adar, E., Delice, E.K., Adar, T., 2022. Prioritizing of industrial wastewater management processes using an integrated AHP–CoCoSo model: Comparative and sensitivity analyses. Int. J. Environ. Sci. Technol. 19 (6), 4691–4712.

Akhgar, M.R., Moradalizadeh, M., Faghihi-Zarandi, A., Rajaei, P., 2011. Chemical composition of the essential oils of ferula oopoda (boiss. & buhse) boiss. and ferula badghysi (korovin.) from iran. J. Essent. Oil Bear. Plants 14 (3), 297–301.

Akhgar, M.R., Shariatifar, M., Akhgar, A.R., Moradalizadeh, M., Faghihi-Zarandi, A., 2012. Chemical composition and antibacterial activity of the leaf essential oil from Hertia intermedia. Chem. Nat. Compd. 48 (2), 329–331.

Albukhari, S.M., Ismail, M., Akhtar, K., Danish, E.Y., 2019. Catalytic reduction of nitrophenols and dyes using silver nanoparticles@ cellulose polymer paper for the resolution of waste water treatment challenges. Colloids Surf. A Physicochem. Eng. Asp. 577, 548–561.

Alibeigi, A.N., N. Javid, M. Amiri Gharaghani, Z. Honarmandrad, and F. Parsaie, *Synthesis, characteristics, and photocatalytic activity of zinc oxide nanoparticles stabilized on the stone surface for degradation of metronidazole from aqueous solution.* Environmental Health Engineering And Management Journal, 2021. **8**(1): p. 55-63.

Amiri Fard, M.H., A. Nasiri, and H. Daraei, *Green synthesis of AgCoFe2O4@ Ch/AC as a recyclable, magnetic nanohybrid heterogeneous catalyst in photodegradation of ceftriaxone from aqueous solutions with effluent bioassay.* Applied Water Science, 2023. **13**(11): p. 220.

Ansari, A.R., Hammad, A.H., Abdel-wahab, M.S., Shariq, M., Imran, M., 2020. Structural, optical and photoluminescence investigations of nanocrystalline CuO thin films at different microwave powers. Opt. Quant. Electron. 52 (10), 426.

Ariga, K., Vinu, A., Yamauchi, Y., Ji, Q., Hill, J.P., 2012. Nanoarchitectonics for mesoporous materials. Bull. Chem. Soc. Jpn. 85 (1), 1–32.

Asenath-Smith, E., Ambrogi, E.K., Barnes, E., Brame, J.A., 2020. CuO enhances the photocatalytic activity of Fe2O3 through synergistic reactive oxygen species interactions. Colloids Surf. A Physicochem. Eng. Asp. 603, 125179.

Azarshab, K., Hashemi, M., Nasiri, A., Khodabakhshi, A., 2024. Synthesis and characterization of CuCoFe2O4@ GA/AC as a bio-based matrix magnetic nano-heterogeneous photocatalyst for ceftriaxone degradation from aqueous media. Appl. Water Sci. 14 (9), 1–24.

Bahnemann, D., Cunningham, J., Fox, M., Pelizzetti, E., Pichat, P., Serpone, N., 2018. Photocatalytic treatment of waters. In: Aquatic and Surface Photochemistry. CRC Press, pp. 261–316.

Bello, M.M., Raman, A.A.A., 2019. Synergy of adsorption and advanced oxidation processes in recalcitrant wastewater treatment. Environ. Chem. Lett. 17, 1125–1142.

Cao, H., M. Wan, Y. Qiao, S. Zhang, and R. Li, *Spatial distribution of sonoluminescence and sonochemiluminescence generated by cavitation bubbles in 1.2 MHz focused ultrasound field.* Ultrasonics sonochemistry, 2012. **19**(2): p. 257-263.

Carta, D., Casula, M.F., Falqui, A., Loche, D., Mountjoy, G., Sangregorio, C., Corrias, A., 2009. A structural and magnetic investigation of the inversion degree in ferrite nanocrystals MFe2O4 (M= Mn Co, Ni). J. Phys. Chem. C 113 (20), 8606–8615.

Chauhan, M., Kaur, N., Bansal, P., Kumar, R., Srinivasan, S., Chaudhary, G.R., 2020. Proficient photocatalytic and sonocatalytic degradation of organic pollutants using CuO nanoparticles. J. Nanomater. 2020, 1–15.

Dehvari, M., Babaei, A.A., Esmaeili, S., 2023. Amplification of oxidative elimination of atrazine by Ultrasound/Ultraviolet–assisted Sono/Photocatalyst using a spinel cobalt ferrite–anchored MWCNT as peroxymonosulfate activator. J. Photochem. Photobiol. A Chem. 437, 114452.

Dong, G., Chen, B., Liu, B., Hounjet, L.J., Cao, Y., Stoyanov, S.R., Yang, M., Zhang, B., 2022. Advanced oxidation processes in microreactors for water and wastewater treatment: Development, challenges, and opportunities. Water Res. 211, 118047.

Elahi, Z., Gull, W., 2024. Indexing the X-ray diffraction patterns of cubic and hexagonal structures using spreadsheets. Spreadsheets Educ. 1–15.

Elreedy, A., Ibrahim, E., Hassan, N., El-Dissouky, A., Fujii, M., Yoshimura, C., Tawfik, A., 2017. Nickel-graphene nanocomposite as a novel supplement for enhancement of biohydrogen production from industrial wastewater containing mono-ethylene glycol. Energ. Conver. Manage. 140, 133–144.

Esmaeili, E., Salavati-Niasari, M., Mohandes, F., Davar, F., Seyghalkar, H., 2011. Modified single-phase hematite nanoparticles via a facile approach for large-scale synthesis. Chem. Eng. J. 170 (1), 278–285.

Fadaei, S., F.N. Moghadam, M. Hashemi, and H. Pourzamani, *BTEX Removal from Aqueous Solution by Modified Multi-Walled Carbon Nanotubes With Ozone.* Anuario do Instituto de Geociencias, 2017. **40**(1).

Farghali, A., Bahgat, M., Allah, A.E., Khedr, M., 2013. Adsorption of Pb (II) ions from aqueous solutions using copper oxide nanostructures. Beni-Suef Univ. J. Basic Appl. Sci. 2 (2), 61–71.

Feichtmeier, N.S., Leopold, K., 2014. Detection of silver nanoparticles in parsley by solid sampling high-resolution–continuum source atomic absorption spectrometry. Anal. Bioanal. Chem. 406, 3887–3894.

Gharaghani, M.A., Samaei, M., Mahdizadeh, H., Nasiri, A., Keshtkar, M., Mohammadpour, A., Khaneghah, A.M., 2024. An effective magnetic nanobiocomposite: Preparation, characterization and its application for adsorption removal of P-nitroaniline from aquatic environments. Environ. Res. 246, 118128.

Gharaghani, M.A., Dehdarirad, A., Mahdizadeh, H., Hashemi, H., Nasiri, A., Samaei, M. R., Mohammadpour, A., 2024. Photocatalytic degradation of Acid Red 18 by synthesized AgCoFe2O4@ Ch/AC: Recyclable, environmentally friendly, chemically stable, and cost-effective magnetic nano hybrid catalyst. Int. J. Biol. Macromol. 269, 131897.

Giahi, M., Pathania, D., Agarwal, S., Ali, G.A., Chong, K.F., Gupta, V.K., 2019. Preparation of Mg-doped TiO2 nanoparticles for photocatalytic degradation of some organic pollutants. Studia UBB Chemia 64 (1), 7–18.

Golbabai, F., Ebrahimi, A., Shirkhanloo, H., Baneshi, M.R., Zarandi, A.F., Kian, M.J., 2013. Performance comparison survey of multi-walled and single-walled carbon nanotubes for adsorption and desorption of mercury vapors in the air. Iran Occupational Health 10 (5), 21–31.

Gui, M.M., Wong, W.M.P., Chai, S.-P., Mohamed, A.R., 2015. One-pot synthesis of Ag-MWCNT@ TiO2 core–shell nanocomposites for photocatalytic reduction of CO2 with water under visible light irradiation. Chem. Eng. J. 278, 272–278.

Haghshenas, M., Mazloum-Ardakani, M., Tamaddon, F., Nasiri, A., 2021. CoFe2O4@ methyl cellulose core-shell nanostructure and their hybrids with functionalized graphene aerogel for high performance asymmetric supercapacitor. Int. J. Hydrogen Energy 46 (5), 3984–3995.

Haghshenas, M., Mazloum-Ardakani, M., Tamaddon, F., Nasiri, A., 2021. CoFe2O4@ methyl cellulose core-shell nanostructure and their hybrids with functionalized graphene aerogel for high performance asymmetric supercapacitor. Int. J. Hydrogen Energy 46 (5), 3984–3995.

Hamidi, Z., Karimi Zarchi, M.A., 2018. Synthesis of polymer-supported Fe 3 O 4 nanoparticles and their application as a novel route for the synthesis of imidazole derivatives. Res. Chem. Intermed. 44, 6995–7011.

Hashemi, H., Rajabi, S., Nikooee, S., Asrari, E., 2023. Ozonation of secondary industrial effluent for beneficial reuse. Desalin. Water Treat. 287, 96–102.

Hassani, A., Khataee, A., Karaca, S., Karaca, C., Gholami, P., 2017. Sonocatalytic degradation of ciprofloxacin using synthesized TiO2 nanoparticles on montmorillonite. Ultrason. Sonochem. 35, 251–262.

Hawash, H.B., Moneer, A.A., Galhoum, A.A., Elgarahy, A.M., Mohamed, W.A., Samy, M., El-Seedi, H.R., Gaballah, M.S., Mubarak, M.F., Attia, N.F., 2023. Occurrence and spatial distribution of pharmaceuticals and personal care products (PPCPs) in the aquatic environment, their characteristics, and adopted legislations. J. Water Process Eng. 52, 103490.

Huang, Y., Xu, W., Hu, L., Zeng, J., He, C., Tan, X., He, Z., Zhang, Q., Shu, D., 2017. Combined adsorption and catalytic ozonation for removal of endocrine disrupting compounds over MWCNTs/Fe3O4 composites. Catal. Today 297, 143–150.

Ighalo, J.O., Sagboye, P.A., Umenweke, G., Ajala, O.J., Omoarukhe, F.O., Adeyanju, C.A., Ogunniyi, S., Adeniyi, A.G., 2021. CuO nanoparticles (CuO NPs) for water treatment: A review of recent advances. Environ. Nanotechnol. Monit. Manage. 15, 100443.

Jaafar, N., Jalil, A., Triwahyono, S., Efendi, J., Mukti, R., Jusoh, R., Jusoh, N., Karim, A., Salleh, N., Suendo, V., 2015. Direct in situ activation of Ag0 nanoparticles in synthesis of Ag/TiO2 and its photoactivity. Appl. Surf. Sci. 338, 75–84.

Jonak, S., Borah, J., 2021. Correlation between cation distribution and heating efficiency of annealed Fe3O4 nanoparticles. Mater. Today Commun. 26, 101789.

Kabel, K.I., Farag, A.A., Elnaggar, E.M., Al-Gamal, A.G., 2016. Removal of oxidation fragments from multi-walled carbon nanotubes oxide using high and low concentrations of sodium hydroxide. Arab. J. Sci. Eng. 41, 2211–2220.

Kahkha, M.R.R., Zarandi, A.F., Shafighi, N., Kosari, S., Kahkha, B.R., 2020. Magnetic bentonite nanocomposite for removal of amoxicillin from wastewater samples using response surface methodology before determination by high performance liquid chromatography. Analyt. Methods Environ. Chem. J. 3 (3), 25–31.
Karami, M., Ghanbari, M., Amiri, O., Salavati-Niasari, M., 2020. Enhanced antibacterial activity and photocatalytic degradation of organic dyes under visible light using cesium lead iodide perovskite nanostructures prepared by hydrothermal method. Sep. Purif. Technol. 253, 117526.
Karami, N., Mohammadpour, A., Samaei, M.R., Amani, A.M., Dehghani, M., Varma, R.S., Sahu, J., 2024. Green synthesis of sustainable magnetic nanoparticles Fe3O4 and Fe3O4-chitosan derived from Prosopis farcta biomass extract and their performance in the sorption of lead (II). Int. J. Biol. Macromol. 254, 127663.
Karami, A., Monsef, R., Waleed, I., Kareem, H.L., Ibrahim, I.T., Salavati-Niasari, M., 2023. Microwave synthesized erbium vanadate nano-photocatalyst: Application for enhanced degradation of contaminated water. Int. J. Hydrogen Energy 48 (23), 8499–8513.
Kasina, A., Cocklin, E., Horswell, S., Grunder, Y., Lucas, C.A., 2024. Structure of the electrochemical interface: Ag (hkl) in an alkaline electrolyte. J. Phys. Chem. C.
Khataee, A., Eghbali, P., Irani-Nezhad, M.H., Hassani, A., 2018. Sonochemical synthesis of WS2 nanosheets and its application in sonocatalytic removal of organic dyes from water solution. Ultrason. Sonochem. 48, 329–339.
Khojasteh, H., Salavati-Niasari, M., Safajou, H., Safardoust-Hojaghan, H., 2017. Facile reduction of graphene using urea in solid phase and surface modification by N-doped graphene quantum dots for adsorption of organic dyes. Diam. Relat. Mater. 79, 133–144.
Kianfar, A.H., Arayesh, M.A., 2020. Synthesis, characterization and investigation of photocatalytic and catalytic applications of Fe3O4/TiO2/CuO nanoparticles for degradation of MB and reduction of nitrophenols. J. Environ. Chem. Eng. 8 (1), 103640.
Kumar, L., Kumar, P., Narayan, A., Kar, M., 2013. Rietveld analysis of XRD patterns of different sizes of nanocrystalline cobalt ferrite. International Nano Letters 3, 1–12.
Kumar, R., Kumar, G., Akhtar, M., Umar, A., 2015. Sonophotocatalytic degradation of methyl orange using ZnO nano-aggregates. J. Alloy. Compd. 629, 167–172.
Lewis, K.A., Tzilivakis, J., Warner, D.J., Green, A., 2016. An international database for pesticide risk assessments and management. Hum. Ecol. Risk Assess. Int. J. 22 (4), 1050–1064.
Low, J., Qiu, S., Xu, D., Jiang, C., Cheng, B., 2018. Direct evidence and enhancement of surface plasmon resonance effect on Ag-loaded TiO2 nanotube arrays for photocatalytic CO2 reduction. Appl. Surf. Sci. 434, 423–432.
Luo, L., Xiao, X., Li, Q., Wang, S., Li, Y., Hou, J., Jiang, B., 2021. Engineering of single atomic Cu-N3 active sites for efficient singlet oxygen production in photocatalysis. ACS Appl. Mater. Interfaces 13 (49), 58596–58604.
Mahdavi, K., Zinatloo-Ajabshir, S., Yousif, Q.A., Salavati-Niasari, M., 2022. Enhanced photocatalytic degradation of toxic contaminants using Dy2O3-SiO2 ceramic nanostructured materials fabricated by a new, simple and rapid sonochemical approach. Ultrason. Sonochem. 82, 105892.
Makuła, P., M. Pacia, and W. Macyk, *How to correctly determine the band gap energy of modified semiconductor photocatalysts based on UV–Vis spectra.* 2018, ACS Publications. p. 6814-6817.
Malakootian, M., Darabi-Fard, Z., Amirmahani, N., Nasiri, A., 2015. Evaluation of arsenic, copper, lead, cadmium, and iron concentration in drinking water resources of central and Southern Bardsir plain, Iran, in 2014. J. Kerman Univ. Med. Sci. 22 (5), 542–554.
Malakootian, M., H. Mahdizadeh, M. Khavari, A. Nasiri, M.A. Gharaghani, M. Khatami, E. Sahle-Demessie, and R.S. Varma, *Efficiency of novel Fe/charcoal/ultrasonic micro-electrolysis strategy in the removal of Acid Red 18 from aqueous solutions.* Journal of Environmental Chemical Engineering, 2020. **8**(2).
Maleky, S., Asadipour, A., Nasiri, A., Luque, R., Faraji, M., 2022. Tetracycline adsorption from aqueous media by magnetically separable Fe3O4@ Methylcellulose/APTMS: Isotherm, kinetic and thermodynamic studies. J. Polym. Environ. 30 (8), 3351–3367.
Maleky, S., Asadipour, A., Nasiri, A., Luque, R., Faraji, M., 2022. Tetracycline adsorption from aqueous media by magnetically separable Fe3O4@Methylcellulose/APTMS: Isotherm, kinetic and thermodynamic studies. J. Polym. Environ. 30 (8), 3351–3367.
Maleky, S., Asadipour, A., Nasiri, A., Luque, R., Faraji, M., 2022. Tetracycline adsorption from aqueous media by magnetically separable Fe3O4@ methylcellulose/APTMS: Isotherm, kinetic and thermodynamic studies. J. Polym. Environ. 1–17.
Margan, P., Haghighi, M., 2018. Sono-coprecipitation synthesis and physicochemical characterization of CdO-ZnO nanophotocatalyst for removal of acid orange 7 from wastewater. Ultrason. Sonochem. 40, 323–332.
Pérez Medina Martínez, V., C.E. Espinosa de la Garza, A.G. Hernández-García, and N.O. Pérez, *Detection and quantification of leached ethylene glycol in biopharmaceuticals by RP-UHPLC.* Analytical and bioanalytical chemistry, 2020. **412**: p. 1795-1806.
Mehdizadeh, A., Derakhshan, Z., Abbasi, F., Samaei, M.R., Baghapour, M.A., Hoseini, M., Lima, E.C., Bilal, M., 2022. The effect of arsenic on the photocatalytic removal of methyl tet butyl ether (MTBE) using Fe2O3/MgO catalyst, modeling, and process optimization. Catalysts 12 (8), 927.
Mirnasab, M., Hashemi, H., Samaei, M., Azhdarpoor, A., 2021. Advanced removal of water NOM by pre-ozonation, enhanced coagulation and bio-augmented granular activated carbon. Int. J. Environ. Sci. Technol. 1–10.
Mondal, P., Nandan, A., Ajithkumar, S., Siddiqui, N.A., Raja, S., Kola, A.K., Balakrishnan, D., 2023. Sustainable application of nanoparticles in wastewater treatment: Fate, current trend & paradigm shift. Environ. Res., 116071
Moradalizadeh, M., Akhgar, M.R., Faghihi-Zarandi, A., 2013. Microwave-assisted and conventional hydrodistillation of essential oils from Apium graveolens L. Asian J. Chem. 25 (1), 79–81.
Moreira, M.D., Neto, N.F.A., Oliveira, F.K., Paskocimas, C.A., Bomio, M.R., Motta, F.V., 2023. Study of the bactericidal properties of ZnO/Ag0 nanoparticles in the treatment of raw sewage effluents. Int. J. Ceram. Eng. Sci. 5 (2), e10173.
Nasiri, A., Malakootian, M., Heidari, M.R., Asadzadeh, S.N., 2021. CoFe2O4@ methylcelloluse as a new magnetic nano biocomposite for sonocatalytic degradation of Reactive Blue 19. J. Polym. Environ. 29 (8), 2660–2675.
Nasiri, A., Heidari, M.R., Javid, N., Yazdanpanah, G., 2022. New efficient and recyclable magnetic nanohybrid adsorbent for the metronidazole removal from simulated wastewater. J. Mater. Sci. Mater. Electron. 33 (33), 25103–25126.
Nasiri, A., Rajabi, S., Hashemi, M., Nasab, H., 2022. CuCoFe2O4@ MC/AC as a new hybrid magnetic nanocomposite for metronidazole removal from wastewater: Bioassay and toxicity of effluent. Sep. Purif. Technol. 296, 121366.
Nasiri, A., Malakootian, M., Javid, N., 2022. Modelling and optimization of lead adsorption by CoFe2 O4 @CMC@HZSM-5 from aqueous solution using response surface methodology. Desalin. Water Treat. 248, 134–148.
Nasiri, A., Rajabi, S., Hashemi, M., Nasab, H., 2022. CuCoFe2O4@ MC/AC as a new hybrid magnetic nanocomposite for Metronidazole removal from wastewater: bioassay and toxicity of effluent. Sep. Purif. Technol., 121366
Nasiri, A., Rajabi, S., Hashemi, M., 2022. CoFe2O4@ methylcellulose/AC as a new, green, and eco-friendly nano-magnetic adsorbent for removal of Reactive Red 198 from aqueous solution. Arab. J. Chem. 15 (5), 103745.
Nasiri, A., Golestani, N., Rajabi, S., Hashemi, M., 2024. Facile and green synthesis of recyclable, environmentally friendly, chemically stable, and cost-effective magnetic nanohybrid adsorbent for tetracycline adsorption. Heliyon 10 (2), e24179.
Okeowo, I.O., Balogun, E.O., Ademola, A.J., Alade, A.O., Afolabi, T.J., Dada, E.O., Farombi, A.G., 2020. Adsorption of phenol from wastewater using microwave-assisted Ag–Au nanoparticle-modified mango seed shell-activated carbon. Int. J. Environ. Res. 14, 215–233.
Panahi, A., Monsef, R., Hussein, S.A., Hammood, S.A., Al-Azzawi, W.K., Raffik, D.E., Hashim, F.S., Salavati-Niasari, M., 2023. Multidisciplinary methods for synthesis of visible-light-driven TmVO4 nanostructure photocatalyst with enhanced photocatalytic activity towards removal of toxic contaminates. Int. J. Hydrogen Energy 48 (85), 33155–33165.
Pathania, D., Sarita, S., Rathore, B.S., 2011. Synthesis, characterization and photocatalytic application of bovine serum albumin capped cadmium sulphide nanopartilces. Chalcogenide Lett. 8 (6), 396–404.
Pathania, D., Gupta, D., Agarwal, S., Asif, M., Gupta, V.K., 2016. Fabrication of chitosan-g-poly (acrylamide)/CuS nanocomposite for controlled drug delivery and antibacterial activity. Mater. Sci. Eng. C 64, 428–435.
Peng, G., Zhang, M., Deng, S., Shan, D., He, Q., Yu, G., 2018. Adsorption and catalytic oxidation of pharmaceuticals by nitrogen-doped reduced graphene oxide/Fe3O4 nanocomposite. Chem. Eng. J. 341, 361–370.
Perlman, O., Weitz, I.S., Azhari, H., 2015. Copper oxide nanoparticles as contrast agents for MRI and ultrasound dual-modality imaging. Phys. Med. Biol. 60 (15), 5767.
Pourshaban-Mazandarani, M. and A. Nasiri, *Photocatalytic Degradation of Tetracycline in Wastewater with Bio-based Matrix Magnetic Heterogeneous Nanocatalyst: Performance and Mechanism Study.* Journal of Polymers and the Environment, 2024: p. 1-25.
Rahimi, F., Nasiri, A., Hashemi, M., Rajabi, S., Abolghasemi, S., 2024. Advances in three-dimensional electrochemical degradation: A comprehensive review on pharmaceutical pollutants removal from aqueous solution. Chemosphere 362, 142620.
Rajabi, S., Nasiri, A., Hashemi, M., 2022. Enhanced activation of persulfate by $CuCoFe_2O_4$@MC/AC as a novel nanomagnetic heterogeneous catalyst with ultrasonic for metronidazole degradation. Chemosphere 286 (3), 131872.
Rajabi, S., Derakhshan, Z., Nasiri, A., Feilizadeh, M., Mohammadpour, A., Salmani, M., Kochaki, S.H., Shouhanian, H., Hashemi, H., 2024. Synergistic degradation of metronidazole and Penicillin G in aqueous solutions using AgZnFe2O4@ chitosan nano-photocatalyst under UV/persulfate activation. Environ. Technol. Innov., 103724
Rajabi, S., Derakhshan, Z., Hashemi, M., Feilizadeh, M., Heidari Kochaki, S., Hashemi, H., Salehi, M., Zare, A., Shourabi, N.S., Moradalizadeh, S., 2024. Metronidazole adsorption by bio-synthesized silver-zinc ferrite nanoadsorbent in presence of chitosan from aqueous media: response surface methodology. Appl. Water Sci. 14 (5), 92.
Ren, H., A. Labidi, A. Sial, T. Gao, X. Xu, J. Liang, H. Kang, Y. Liao, K. Zhao, and M. Padervand, *Carbon quantum dots modified Z and S–Scheme heterojunctions for pharmaceutical contaminants photodegradation: State–of–the–art, benefits, and limitations.* Separation and Purification Technology, 2024: p. 127508.
Rodrigues Filho, G., R.M. de Assunção, J.G. Vieira, C.d.S. Meireles, D.A. Cerqueira, H. da Silva Barud, S.J. Ribeiro, and Y. Messaddeq, *Characterization of methylcellulose produced from sugar cane bagasse cellulose: Crystallinity and thermal properties.* Polymer degradation and stability, 2007. **92**(2): p. 205-210.
Rong, Y., Jin, M., Du, Q., Shen, Z., Feng, Y., Wang, M., Li, F., Liu, R., Li, H., Chen, C., 2022. Simultaneous ambient long-term conductivity promotion, interfacial modification, ion migration inhibition and anti-deliquescence by MWCNT: NiO in spiro-OMeTAD for perovskite solar cells. J. Mater. Chem. A 10 (42), 22592–22604.
Sabok-khiz, Z., Nasiri, A., Daraei, H., 2024. Ceftriaxone photodegradation in wastewater using AgCuFe2O4/ZnO Almond-like heterogeneous nanocatalyst anchored on multi walled carbon nanotubes: Synthesis, characterization, mechanism study, and bioassay effluent. Environ. Technol. Innov., 103759
Salavati-Niasari, M., 2006. Ship-in-a-bottle synthesis, characterization and catalytic oxidation of styrene by host (nanopores of zeolite-Y)/guest ([bis (2-hydroxyanil) acetylacetonato manganese (III)]) nanocomposite materials (HGNM). Micropor. Mesopor. Mater. 95 (1–3), 248–256.
Salavati-Niasari, M., Dadkhah, M., Davar, F., 2009. Pure cubic ZrO2 nanoparticles by thermolysis of a new precursor. Polyhedron 28 (14), 3005–3009.

Sarode, H., Barai, D., Bhanvase, B., Ugwekar, R., Saharan, V., 2020. Investigation on preparation of graphene oxide-CuO nanocomposite based nanofluids with the aid of ultrasound assisted method for intensified heat transfer properties. Mater. Chem. Phys. 251, 123102.
Sekiguchi, Y., Sawatari, C., Kondo, T., 2003. A gelation mechanism depending on hydrogen bond formation in regioselectively substituted O-methylcelluloses. Carbohydr. Polym. 53 (2), 145–153.
Sharma, A., Siddiqi, Z.-M., Pathania, D., 2017. Adsorption of polyaromatic pollutants from water system using carbon/ZnFe2O4 nanocomposite: equilibrium, kinetic and thermodynamic mechanism. J. Mol. Liq. 240, 361–371.
Shirkhanloo, H., Faghihi-Zarandi, A., Mobarake, M.D., 2021. Thiol modified bimodal mesoporous silica nanoparticles for removal and determination toxic vanadium from air and human biological samples in petrochemical workers. NanoImpact 23.
Shirkhanloo, H., Golbabaei, F., Vahid, A., Faghihi Zarandi, A., 2022. A novel nano-palladium embedded on the mesoporous silica nanoparticles for mercury vapor removal from air by the gas field separation consolidation process. Appl. Nanosci. (Switzerland) 12 (5), 1667–1682.
Singh, S.J., Lim, Y.Y., Hmar, J.J.L., Chinnamuthu, P., 2022. Temperature dependency on Ce-doped CuO nanoparticles: a comparative study via XRD line broadening analysis. Appl. Phys. A 128 (3), 188.
Soleimani, E., Moghaddami, R., 2018. Synthesis, characterization and thermal properties of PMMA/CuO polymeric nanocomposites. J. Mater. Sci. Mater. Electron. 29, 4842–4854.
Soleymani, D., Zargari, S., Faghihi-Zarandi, A., 2020. Separation and determination of mercury from nail and hair in petrochemical workers based on silver carbon nanotubes by microwave-assisted headspace sorbent trap. Analyt. Methods Environ. Chem. J. 3 (2), 21–33.
Song, J., Jiang, C., Liu, Z., Yang, Z., Wang, Z., Jiang, Q., Ruuskanen, P., 2023. Drastic performance enhancement of photoluminescence and water electrolysis by local-magnetic-field-assisted LSPR of Ag NPs and NCs. Colloids Surf. A Physicochem. Eng. Asp. 665, 131215.
Tripathi, S., Purchase, D., Chandra, R., Nadda, A.K., Chaturvedi, P., 2023. Emerging pollutants characterization, mitigation and toxicity assessment of sewage wastewater treatment plant-India: A case study. J. Contam. Hydrol. 254, 104139.
Wang, J., Xia, Y., Dong, Y., Chen, R., Xiang, L., Komarneni, S., 2016. Defect-rich ZnO nanosheets of high surface area as an efficient visible-light photocatalyst. Appl. Catal. B: Environ. 192, 8–16.
Xu, L., An, H.-L., Wu, X.-Q., Ju, W.-T., Wang, Y., Wang, X.-F., Wang, X., 2023. Sonocatalytic degradation of tetracycline by Cu2O/MgFe2O4 nanocomposites: Operational parameters, sonocatalytic mechanism, degradation pathways, and environmental toxicity. Surf. Interfaces 41, 103202.
Yahya, N., Aziz, F., Jamaludin, N., Mutalib, M., Ismail, A., Salleh, W., Jaafar, J., Yusof, N., Ludin, N., 2018. A review of integrated photocatalyst adsorbents for wastewater treatment. J. Environ. Chem. Eng. 6 (6), 7411–7425.
Yang, P., Li, S., Xiaofu, L., Xiaojing, A., Liu, D., Huang, W., 2022. Singlet oxygen-dominated activation of peroxymonosulfate by CuO/MXene nanocomposites for efficient decontamination of carbamazepine under high salinity conditions: Performance and singlet oxygen evolution mechanism. Sep. Purif. Technol. 285, 120288.
Yazdanpanah, G., Heidari, M.R., Amirmahani, N., Nasiri, A., 2023. Heterogeneous Sono-Fenton like catalytic degradation of metronidazole by Fe3O4@HZSM-5 magnetite nanocomposite. Heliyon 9 (6).
Yeganeh-Faal, A., Kadkhodaei, M., 2022. A new combustion method for the synthesis of copper oxide nano sheet and Fe3O4/CuO magnetic nanocomposite and its application in removal of diazinon pesticide. Results Eng. 16, 100599.
Yeshchenko, O.A., Dmitruk, I.M., Alexeenko, A.A., Kotko, A.V., Verdal, J., Pinchuk, A.O., 2012. Size and temperature effects on the surface plasmon resonance in silver nanoparticles. Plasmonics 7, 685–694.
Zarandi, A.F., Shirkhanloo, H., Paydar, P., 2020. A novel method based on functionalized bimodal mesoporous silica nanoparticles for efficient removal of lead aerosols pollution from air by solid-liquid gas-phase extraction 03 Chemical Sciences 0306 Physical Chemistry (incl. Structural). J. Environ. Health Sci. Eng. 18 (1), 177–188.
Zhang, J., Zhao, Y., Zhang, K., Zada, A., Qi, K., 2023. Sonocatalytic degradation of tetracycline hydrochloride with CoFe2O4/g-C3N4 composite. Ultrason. Sonochem. 94, 106325.
Zhu, L., Meng, Z.-D., Park, C.-Y., Ghosh, T., Oh, W.-C., 2013. Characterization and relative sonocatalytic efficiencies of a new MWCNT and CdS modified TiO2 catalysts and their application in the sonocatalytic degradation of rhodamine B. Ultrason. Sonochem. 20 (1), 478–484.
Zinatloo-Ajabshir, S., Salehi, Z., Amiri, O., Salavati-Niasari, M., 2019. Simple fabrication of Pr2Ce2O7 nanostructures via a new and eco-friendly route; a potential electrochemical hydrogen storage material. J. Alloy. Compd. 791, 792–799.